

# Equivalent layer technique: an extended review and new contributions

Vanderlei C. Oliveira Jr.<sup>1</sup> and Valéria C. F. Barbosa<sup>1</sup>

<sup>1</sup> *Observatório Nacional, Rio de Janeiro, Brazil*

*e-mails: vandscoelho@gmail.com, valcris@on.br*

(January 4, 2016)

**GEO-2015-XXXX**

Running head: **Equivalent layer technique**

## ABSTRACT

Equivalent layer technique is a powerful tool for processing potential-field data (e.g., interpolation, reduction to the pole, upward and downward continuations). We present a broad review of the equivalent layer technique including an in-depth review of its mathematical foundations, in both the continuous and discrete cases, and its physical meaning. We present a review of the classical equivalent technique and we show mathematically that some of data processing depend on the physical-property distribution estimated over the equivalent layer. We address this dependence through the equation of the predicted magnetic data produced by an equivalent layer composed by a set of dipoles. We review in-depth the computation aspects of the equivalent technique showing how the authors in the literature have been dealt with the high computational cost of this large-scaled problem. By using the floating-point operations, we graphically show the computational demands in using the equivalent layer technique. We review the theoretical aspects concerning the estimated physical-property

distribution within an equivalent layer. We generalize, in the space domain, the relationship between the magnetic moment distribution within a planar equivalent layer and the gravity data. We prove that a positive physical-property distribution within an equivalent layer exists even if the magnetic data are produced by remanent magnetization. Applications to synthetic data intend to illustrate some processing of potential-field data that depend on the physical-property distribution (e.g., reduction to the pole) and the ones that do not depend on (e.g., upward continuation and interpolation).

## INTRODUCTION

Equivalent layer technique appeared in the geophysical literature over 50 years ago and have been used as a tool to process potential-field data such as interpolation (e.g., Cordell, 1992; Mendonça and Silva, 1994), upward (or downward) continuation (e.g., Emilia, 1973; Hansen and Miyazaki, 1984; Li and Oldenburg, 2010) reduction to the pole of magnetic data (e.g., Silva, 1986; Leão and Silva, 1989; Guspí and Novara, 2009; Oliveira Jr. et al., 2013) and gradient data (Barnes and Lumley, 2011).

The equivalent layer technique is grounded on potential theory, which is the theory of a certain differential equation known as Laplace's equation. Mathematically, a solution of Laplace's equation is called a harmonic function (Kellogg, 1929). A function  $U(x, y, z)$  at a point  $P(x, y, z)$  is harmonic if its second derivatives exist and are continuous and satisfy Laplace's equation throughout some neighborhood of that point (Kellogg, 1929). A well-known tool for deriving and understanding properties of harmonic functions is a set of Green's identities (Kellogg, 1929). In accordance with potential theory, a discrete set of observations of a potential field produced by any source can be exactly reproduced by a continuous and infinite 2D physical-property surface distribution. This distribution is named equivalent layer, which is a fictitious layer of sources, located below the observation plane that yields a field that satisfies Laplace's equation and reproduces observed potential-field data. The equivalent layer is a consequence of solving the Laplace's equation in the source-free region above the observation surface using the observed field as the Dirichlet boundary condition.

There is no controversy whatsoever that the authorship of the equivalent layer principle is George Green in 1828. On the other hand, it was not used until the 1960s by the geo-

physicists. In the 1960s, several authors in geophysical literature used the terms equivalent layer and equivalent sources. Roy (1962) uses the term Greens theorem of equivalent layer to draw attention that the observed potential field data can be exactly reproduced by an infinite number of surface physical-property distribution. Dampney (1969) uses the term equivalent layer to define a fictitious stratum located below the observation surface and with finite horizontal dimensions which is composed by a finite discrete set of equivalent sources. To our knowledge, such approximation of the continuous equivalent layer by a discrete layer has not been previously applied to potential-field data. In the timeline for magnetic methods of exploration proposed by Nabighian et al. (2005b), the event of the equivalent-source technique was assigned to Dampney (1969). However, Dampney (1969) recognized that the idea of an equivalent layer has been exploited by other authors such as Daneš (1962), Zidarov (1965) and Bott (1967).

In the beginning, the equivalent layer technique was predominantly used in processing and in interpreting potential-field data. Emilia (1973) showed a wide use of equivalent layer technique in magnetic data processing such as the first and second vertical derivatives, the upward and downward continuations and the reduction to the pole. To our knowledge, Emilia (1973) is the pioneer on the use of the equivalent layer technique in the wavenumber domain by computing the band-pass filtered data and the amplitude spectrum of the data. Emilia (1973) also pointed out that the equivalent layer technique could be used to compute the horizontal and vertical field components, higher-order vertical derivatives, horizontal derivatives, and power and phase spectra.

After Emilia (1973), the equivalent layer technique was used to perform other transformations and to deal with 3D potential-field data. Bott and Ingles (1972) used Poisson theorem and the equivalent layer technique to compute the pseudogravimetric and pseudo-

magnetic transformations and to estimate the direction of magnetization and the ratio of magnetization to density. Silva (1986) used the equivalent layer technique to perform a reduction to the pole of 3D magnetic data at low magnetic latitudes. By using the equivalent layer technique Cordell (1992) and Mendonça and Silva (1994), proposed two schemes to interpolate the 3D potential-field data. Recently, Barnes and Lumley (2011) and Barnes (2014) used the equivalent layer technique to process airborne full-tensor gravity gradient data.

Since the late 1970s, the equivalent layer technique has been widely used in processing satellite data. To our knowledge, Mayhew (1982) was the pioneer on the use of equivalent layer in satellite-data processing. Instead of processing satellite data by spherical harmonics or Fourier transform methods, Von Frese et al. (1981) used the equivalent layer technique to estimate a spherical distribution of equivalent point sources for processing of both gravity and magnetic anomalies in spherical coordinates system and applied it to obtain geoidal anomalies, pseudoanomalies, vector anomaly components, spatial derivatives, continuations and magnetic pole reductions.

In the wavenumber domain, Emilia (1973) estimated an equivalent source distribution of line of dipoles and, by using the analytical expression of the line of dipoles, the band-pass filtered data and the amplitude spectrum of the data were analytically computed. To calculate a potential field data on a horizontal plane in the wavenumber domain, Pilkington and Urquhart (1990)'s method consists of two steps. In the first one, an equivalent source distribution that fits the data is estimated on a mirror image of the observation surface. In the second step, this irregular mirror image surface is replaced by a horizontal plane and the potential-field data yielded by the equivalent source is computed on the horizontal plane. Pawlowski (1994) proposed a filtering scheme for regional-residual separation method for

potential-field data which computes the power spectrum of the data by using two equivalent-source layers to model the residual and regional fields. One equivalent layer models the residual data presumably produced by shallower geologic sources and another one models the regional data presumably produced by deeper sources. However, the first complete work of equivalent layer method in wavenumber was presented by Xia et al. (1993) who also proposed a fast interactive scheme of updating the equivalent source distribution.

Despite the equivalent layer concept be grounded on well-established potential-field theory, the theoretical aspects of this method have received little attention. By using the analytical relationship between the potential-field data and equivalent physical-property distribution on an arbitrary observational surface, Bhattacharyya and Chan (1977) proposed an iterative scheme for continuing the potential field data between general surface (e.g., from the flight surface to the draped surface). Hansen and Miyazaki (1984) also used the equivalent layer method to accomplish the continuation of the data between arbitrary surfaces. Pedersen (1991) discussed the relationship between potential fields (pseudogravity and magnetic fields) and some equivalent sources (thin sheets and magnetized half-spaces). In the wavenumber domain, Li et al. (2014) proved that a positive physical property distribution on an equivalent layer exists when the magnetic data are produced by normal induced magnetization. These authors showed that by imposing the positivity constraint on the estimates of the physical-property distribution is sufficient to overcome the low-latitude instability (undesirable artifact of striations) to reduce the magnetic data to the pole using equivalent layer method. MacLennan and Li (2013) developed a method for denoising electric field data from frequency-domain controlled-source electromagnetic (CSEM) surveys using an equivalent layer method.

In comparison with the processing potential-field data using the fast Fourier transform

(Gunn, 1975), the equivalent layer technique has several advantages. These advantages are: 1) the data do not need to be extrapolated beyond the range of observations (Cordell and Grauch, 1982); 2) the data do not need to be equally spaced and; 3) the data do not need to be measured on a plane at constant height. However, one serious disadvantage to the application of the equivalent layer technique is the computational cost. For processing large-potential-field data sets via the equivalent layer technique, the computation cost demanded for building the linear system and for solving the linear inverse problem becomes increasingly important. Several cost-effective methods have developed for processing. In Leão and Silva (1989), the equivalent layer technique is accomplished through a moving-data window and a moving-equivalent-source window which sweep the whole data set. In this fast data-window scheme, the desired transformed data is only computed at the data window center. Xia et al. (1993) developed, in the wavenumber domain, a fast interactive scheme of updating the equivalent source distribution. To compress the linear system of equations associated with the equivalent layer technique, Li and Oldenburg (2010) used a wavelet compression and Davis and Li (2011) combined an adaptive mesh and wavelet compression. Following the tendency of dealing with large data sets, some methods reduced the number of equivalent sources. Barnes and Lumley (2011) do not compute the full sensitivity matrix of the linear system; rather, for each original  $i$ th row, a set of equivalent sources that lie distant from the  $i$ th observation will be grouped together forming an average equivalent source. Oliveira Jr. et al. (2013) assumed that the physical-property distribution within the equivalent layer can be approximated by a piecewise-polynomial function defined on a set of equivalent-source windows. This procedure leads to a drastic reduction of the linear system of equations that needs to be solved for estimating the physical-property distribution within an equivalent layer.

This article reviews the theoretical bases of the equivalent layer technique and its use in processing potential field data. This tutorial starts describing the underlying assumptions for the use of this technique in gravity and magnetic data. Next, we discuss the mathematical foundations of the equivalent layer principle by using the Greens identities to prove the basic equation of the equivalent layer technique called the upward continuation integral. Then, we analyse the classical approach of the equivalent layer technique stressing its physical meaning and translating its mathematical foundation into a context of its practical use. In terms of practical applications of the equivalent layer technique we address the following issues: 1) the build of the discrete equivalent layer; 2) the definition of the harmonic functions; and 3) the computation aspects. We also review the theoretical aspects concerning the equivalent layer. We deduce, in the space domain, a relationship between the magnetic moment distribution within a planar equivalent layer and the pseudogravity on the equivalent layer. To our knowledge, this relationship generalizes the previous ones deduced by Pedersen (1991) and Li et al. (2014) in three aspects. First, it does not impose an induced magnetization of the equivalent sources within the equivalent layer. Second, it does not assume that the observed magnetic anomaly is produced by a purely induced magnetization. Third, it does not consider the observed total-field anomaly on a horizontal plane. Finally in this review, we present tests with synthetic data to evaluate the performance of the equivalent layer technique in processing potential-field data in the cases that the transformation depends on the physical property distribution or not.



## POTENTIAL-FIELD DATA

### Gravity data

The resultant of gravitational force and centrifugal force acting on a body at rest on the Earth's surface is called gravity vector and its intensity is commonly called gravity (Hofmann-Wellenhof and Moritz, 2005), which is the physical quantity usually measured in land gravimetry. In the case of gravimetry on moving platforms (e.g., airplanes, helicopters, marine vessels), there are also additional non-gravitational accelerations due to the vehicle motion like Coriolis acceleration and high-frequency vibrations (Glennie et al., 2000; Nabighian et al., 2005a; Baumann et al., 2012). The geophysicists are usually interested in the gravitational component of gravity, which is a function of the density distribution of geological structures located in subsurface. For convenience, let us denote these density distributions as gravity sources. The gravity sources can be a massive cap rock over a salt dome, the basement relief under sedimentary basins or a sulphide ore body, for example. By properly removing the non-gravitational effects also time variations produced by Earth tides, instrumental drift and barometric pressure changes, for example, the gravity can be considered as the intensity of the gravitational attraction exerted by gravity sources.

The difference between the observed gravity and the intensity of the reference gravity field (e.g., the normal gravity), at the same point, is called gravity disturbance, which is a function of the density distribution of the gravity sources only. The Free-air and Bouguer anomalies (which are gravity anomalies) approximate, respectively, the gravity disturbance and the terrain corrected gravity disturbance. As properly pointed out by Hackney and Featherstone (2003), the gravity disturbance may be more useful and conceptually more logical for geophysical investigations than gravity anomalies. However, many geophysicists

still use the gravity anomalies instead of the gravity disturbance.

In a local- or regional-gravity study, the gravity disturbance  $\delta g_i$ , at the point  $(x_i, y_i, z_i)$ ,  $i = 1, \dots, N$ , can be considered as the  $z$ -component (or vertical component) of the gravitational attraction exerted by gravity sources. In this case, the gravity disturbance produced by a geological body with constant density  $\rho$  can be represented by the following harmonic function

$$\delta g_i = c_g \rho \partial_z \phi_i, \quad (1)$$

where  $c_g = k_g G$ ,  $G$  is the Newtonian constant of gravitation in  $m^3/(kg\ s^2)$ ,  $k_g = 10^5$  is a constant factor transforming the gravity disturbance from  $m/s^2$  to milligal (mGal), and  $\partial_z \phi_i$  is a harmonic function representing the first derivative, evaluated at the observation point  $(x_i, y_i, z_i)$ ,  $i = 1, \dots, N$ , of the function

$$\phi(x, y, z) = \int \int \int_v \frac{1}{\sqrt{(x - x')^2 + (y - y')^2 + (z - z')^2}} dv \quad (2)$$

with respect to the variable  $z$ . In this case, the integral is conducted over the coordinates  $x'$ ,  $y'$  and  $z'$  within the volume  $v$  of the gravity source. In this work, this function is also used to describe the magnetic source and thus the integral is conducted over the volume of the magnetic source. From now on, we use a Cartesian coordinate system with the  $x$  axis pointing to North, the  $y$  axis pointing to East and the  $z$  axis pointing downward.

## Magnetic data

Local distortions of the main geomagnetic field are commonly called total-field anomalies (Nabighian et al., 2005b; Blakely, 1996). They are produced by magnetized bodies located in the subsurface, which are conveniently denominated by magnetic sources. For local- or regional-scale magnetic studies conducted in a short period of time, it is possible to consider

the geomagnetic field as a vector  $\mathbf{F}_0$  with constant direction throughout the study area. In this case,  $\mathbf{F}_0$  can be written as

$$\mathbf{F}_0 = \|\mathbf{F}_0\| \hat{\mathbf{F}}, \quad (3)$$

where  $\|\cdot\|$  denotes the Euclidean norm and

$$\hat{\mathbf{F}} = \begin{bmatrix} \cos(I_0) \cos(D_0) \\ \cos(I_0) \sin(D_0) \\ \sin(I_0) \end{bmatrix}_{3 \times 1} \quad (4)$$

is a unit vector with the same constant inclination  $I_0$  and declination  $D_0$  of the local-geomagnetic field.

The Euclidean norm of  $\mathbf{F}_0$  is generally many times greater than the Euclidean norm of the magnetic induction produced by the magnetic sources at all observation points on the study area (Blakely, 1996). From these assumptions, the observed total-field anomaly  $\Delta T_i^o$ , at the point  $(x_i, y_i, z_i)$ ,  $i = 1, \dots, N$ , can be described by the following harmonic function:

$$\Delta T_i^o = \hat{\mathbf{F}}^\top \mathbf{B}_i, \quad (5)$$

where  $\mathbf{B}_i$  represents the magnetic induction produced by the magnetic sources at the point  $(x_i, y_i, z_i)$ ,  $i = 1, \dots, N$ .

Let's consider a uniformly magnetized source with volume  $v$  and constant magnetization vector  $\mathbf{m}$ . Here, the magnetization intensity is given in ampere per meter (A/m) and the coordinates in meter (m). The magnetic induction  $\mathbf{B}_i$  produced by this source at the point  $(x_i, y_i, z_i)$ ,  $i = 1, \dots, N$ , can be represented as follows:

$$\mathbf{B}_i = c_m \mathbf{M}_i \mathbf{m}, \quad (6)$$

where  $c_m = \frac{\mu_0}{4\pi} k_m$ ,  $\mu_0 = 4\pi \cdot 10^{-7}$  H/m is the magnetic constant,  $k_m = 10^9$  is a constant factor transforming the magnetic induction from Tesla (T) to nanotesla (nT), and  $\mathbf{M}_i$  is a

matrix given by

$$\mathbf{M}_i = \begin{bmatrix} \partial_{xx}\phi_i & \partial_{xy}\phi_i & \partial_{xz}\phi_i \\ \partial_{xy}\phi_i & \partial_{yy}\phi_i & \partial_{yz}\phi_i \\ \partial_{xz}\phi_i & \partial_{yz}\phi_i & \partial_{zz}\phi_i \end{bmatrix}_{3 \times 3}, \quad (7)$$

with  $\partial_{\alpha\beta}\phi_i$ ,  $\alpha = x, y, z$ ,  $\beta = x, y, z$ , being the second derivatives, evaluated at the coordinates  $(x_i, y_i, z_i)$ ,  $i = 1, \dots, N$ , of the function  $\phi(x, y, z)$  (equation 2) with respect to the variables  $x, y$  and  $z$ . In this case, this integral in equation 2 is evaluated over the coordinates  $x', y'$  and  $z'$  within the volume  $v$  of the magnetic source. Finally, by using the magnetic induction  $\mathbf{B}_i$  (equation 6) with the magnetization vector  $\mathbf{m} = m \hat{\mathbf{m}}$ , the observed total-field anomaly  $\Delta T_i^o$  (equation 5) can be rewritten as follows:

$$\Delta T_i^o = c_m m \hat{\mathbf{F}}^\top \mathbf{M}_i \hat{\mathbf{m}}, \quad (8)$$

where  $m$  the magnetization intensity and  $\hat{\mathbf{m}}$  is a unit vector.

## MATHEMATICAL FOUNDATIONS

Let  $v$  be a regular region with boundary defined by a regular surface  $S$  (Figure 1). Let's also consider a regular and continuous scalar function  $U(x, y, z)$ , which is zero at infinite, has continuous first derivatives in  $v$  and also has continuous second derivatives in the interior of  $v$ . In this case, according to the Green's third identity (Kellogg, 1929),

$$U(x_i, y_i, z_i) = -\frac{1}{4\pi} \iiint_v \frac{1}{r} \nabla^2 U(x, y, z) dv - \frac{1}{4\pi} \iint_S U(x, y, z) \partial_n \frac{1}{r} - \frac{1}{r} \partial_n U(x, y, z) dS \quad (9)$$

where the variables  $x_i, y_i$  and  $z_i$  are the Cartesian coordinates of an arbitrarily fixed point within  $v$  (Figure 1). In equation 9, the integrals are conducted over the variables  $x, y$  and  $z$ , which represent either a volume element of  $v$  or an area element of  $S$ . The terms on the

right side of equation 9 are

$$\frac{1}{r} \equiv \frac{1}{\sqrt{(x - x_i)^2 + (y - y_i)^2 + (z - z_i)^2}} , \quad (10)$$

which is the inverse distance from the fixed point  $(x_i, y_i, z_i)$  (black dot in Figure 1) to the integration point  $(x, y, z)$ , the Laplacian of the function  $U(x, y, z)$ , which is given by

$$\nabla^2 U(x, y, z) = \partial_{xx}^2 U(x, y, z) + \partial_{yy}^2 U(x, y, z) + \partial_{zz}^2 U(x, y, z) , \quad (11)$$

where  $\partial_{\alpha\beta}^2 U(x, y, z) \equiv \frac{\partial^2 U(x, y, z)}{\partial\alpha\partial\beta}$ ,  $\alpha, \beta = x, y, z$ , and the normal derivatives

$$\partial_n \frac{1}{r} \equiv \nabla \frac{1}{r} \cdot \hat{\mathbf{n}} \quad (12)$$

and

$$\partial_n U(x, y, z) \equiv \nabla U(x, y, z) \cdot \hat{\mathbf{n}} . \quad (13)$$

In equations 12 and 13, the symbol  $(\cdot)$  denotes the dot product of vectors,  $\hat{\mathbf{n}}$  is the outward-pointing normal to the surface  $S$  at a point  $(x, y, z)$  and, finally,  $\nabla \frac{1}{r}$  and  $\nabla U(x, y, z)$  represent, respectively, the gradient of the functions  $\frac{1}{r}$  (equation 10) and  $U(x, y, z)$ , both with respect to the variables  $x, y$  and  $z$ . By considering that  $U(x, y, z)$  is harmonic at all points  $(x, y, z)$  within  $v$ , the Green's third identity (equation 9) can be rewritten as

$$U(x_i, y_i, z_i) = -\frac{1}{4\pi} \iint_S U(x, y, z) \partial_n \frac{1}{r} - \frac{1}{r} \partial_n U(x, y, z) dS . \quad (14)$$

Notice that, in equation 14, the variables  $x, y$  and  $z$  represent the Cartesian coordinates of an arbitrary point belonging to the surface  $S$  (Figure 1).

Let's split the surface  $S$  into two surfaces  $S_1$  and  $S_2$ , where  $S_1$  is a hemisphere with radius  $R$  and  $S_2$  is a horizontal plane with constant vertical coordinate  $z = z_c$  (Figure 2). We stress that these two surfaces do not have any relationship with the equipotential

surfaces of the harmonic function  $U(x, y, z)$ . In this case, the surface integral can also be split as follows

$$U(x_i, y_i, z_i) = I_1 + I_2, \quad (15)$$

where

$$I_1 = -\frac{1}{4\pi} \iint_{S_1} U(x, y, z) \partial_n \frac{1}{r} - \frac{1}{r} \partial_n U(x, y, z) dS_1 \quad (16)$$

and

$$I_2 = -\frac{1}{4\pi} \iint_{S_2} U(x, y, z_c) \partial_z \frac{1}{r} - \frac{1}{r} \partial_z U(x, y, z_c) dS_2. \quad (17)$$

Notice that, in equation 16, the outward normal  $\hat{\mathbf{n}} = \hat{\mathbf{n}}_1$  (Figure 2) has a constant radial direction whereas, in equation 17, the outward normal  $\hat{\mathbf{n}} = \hat{\mathbf{n}}_2$  (Figure 2) has the same direction as the vertical axis  $z$ , so that  $\partial_n = \partial_z$ . By making  $R \rightarrow \infty$ , the integral on the surface  $S_1$  (equation 16) vanishes and, consequently, equation 15 reduces to

$$U(x_i, y_i, z_i) = -\frac{1}{4\pi} \int_{-\infty}^{+\infty} \int_{-\infty}^{+\infty} U(x, y, z_c) \partial_z \frac{1}{r} - \frac{1}{r} \partial_z U(x, y, z_c) dx dy, \quad (18)$$

where  $z_i = z_c - \Delta z$ , with  $\Delta z > 0$  (Figure 2). Equation 18 shows that, given the values of a harmonic function and its vertical derivative on a horizontal plane at  $z = z_c$ , it is possible to calculate the value of this harmonic function at any point located above this horizontal plane. For practical purposes, it is convenient to manipulate equation 18 in order to remove the vertical derivative  $\partial_z U(x, y, z_c)$ . To do this, let's first define the function

$$\frac{1}{\ell} \equiv \frac{1}{\sqrt{(x - x_i)^2 + (y - y_i)^2 + (z - z_s)^2}} \quad (19)$$

representing the inverse distance between the point  $(x_i, y_i, z_s)$  and an arbitrary point on the plane  $S_2$  (Figure 2). Notice that the point  $(x_i, y_i, z_s)$  (open dot in Figure 2) can be considered a mirror of the point  $(x_i, y_i, z_i)$  (black dot in Figure 2) with respect to the horizontal plane  $S_2$  because  $z_s = z_c + \Delta z$  and  $z_i = z_c - \Delta z$ . Besides,  $\frac{1}{\ell}$  (equation 19) is

harmonic at all points  $(x, y, z)$  in  $v$ . Then, by applying the Green's second identity (Kellogg, 1929), we obtain

$$\iiint_v U(x, y, z) \nabla^2 \frac{1}{\ell} - \frac{1}{\ell} \nabla^2 U(x, y, z) dv = \iint_S U(x, y, z) \partial_n \frac{1}{\ell} - \frac{1}{\ell} \partial_n U(x, y, z) dS. \quad (20)$$

By multiplying both sides in equation 20 by  $1/4\pi$  and recalling that  $U(x, y, z)$  and  $\frac{1}{\ell}$  are harmonic at all points within  $v$ , we have

$$0 = \frac{1}{4\pi} \iint_S U(x, y, z) \partial_n \frac{1}{\ell} - \frac{1}{\ell} \partial_n U(x, y, z) dS \quad (21)$$

and, subsequently, by adding equation 21 to equation 14 we get

$$U(x_i, y_i, z_i) = -\frac{1}{4\pi} \iint_S U(x, y, z) \left( \partial_n \frac{1}{r} - \partial_n \frac{1}{\ell} \right) - \left( \frac{1}{r} - \frac{1}{\ell} \right) \partial_n U(x, y, z) dS. \quad (22)$$

Now, similarly to what was previously done, let's split the surface  $S$  into two surfaces  $S_1$  and  $S_2$ , according to the Figure 2, and let's also tend  $R$  to infinite. Consequently, the integral over the surface  $S_1$  vanishes and equation 22 becomes

$$U(x_i, y_i, z_i) = -\frac{1}{4\pi} \int_{-\infty}^{+\infty} \int_{-\infty}^{+\infty} U(x, y, z_c) \left( \partial_z \frac{1}{r} - \partial_z \frac{1}{\ell} \right) - \left( \frac{1}{r} - \frac{1}{\ell} \right) \partial_z U(x, y, z_c) dx dy. \quad (23)$$

The two terms between parenthesis in the surface integral shown in equation 23 deserve special attention because they assume specific values on this plane. Notice that the derivative of the functions  $\frac{1}{r}$  (equation 10) and  $\frac{1}{\ell}$  (equation 19) with respect to the variable  $z$  are:

$$\partial_z \frac{1}{r} = \frac{-(z - z_i)}{[(x - x_i)^2 + (y - y_i)^2 + (z - z_i)^2]^{\frac{3}{2}}} \quad (24)$$

and

$$\partial_z \frac{1}{\ell} = \frac{-(z - z_s)}{[(x - x_i)^2 + (y - y_i)^2 + (z - z_s)^2]^{\frac{3}{2}}}. \quad (25)$$

Then, by evaluating equations 10, 19, 24 and 25 at a point  $(x, y, z)$ , with  $z = z_c$ , and recalling that  $z_i = z_c - \Delta z$  and  $z_s = z_c + \Delta z$  (Figure 2), we can easily verify that  $\frac{1}{r} = \frac{1}{\ell}$

and  $\partial_z(1/r) = -\partial_z(1/\ell)$ . Consequently, equation 23 can be rewritten as

$$U(x_i, y_i, z_i) = \frac{z_c - z_i}{2\pi} \int_{-\infty}^{+\infty} \int_{-\infty}^{+\infty} \frac{U(x, y, z_c)}{[(x_i - x)^2 + (y_i - y)^2 + (z_i - z_c)^2]^{\frac{3}{2}}} dx dy, \quad z_c > z_i. \quad (26)$$

In the geophysical literature, several authors have presented different versions of equation 26 (Skeels, 1947; Henderson and Zietz, 1949; Henderson, 1960; Roy, 1962; Bhattacharyya, 1967; Henderson, 1970; Twomey, 1977; Blakely, 1996). Here, by following Henderson (1960, 1970), we define equation 26 as the upward continuation integral. This equation is the basis for the equivalent layer technique, which is presented in the next section.

## EQUIVALENT LAYER TECHNIQUE

### Physical meaning and its practical implications

In geophysics, equation 26 is commonly applied for calculating, for example, the upward continuation of potential-field data. We emphasize that the use of this equation implicitly assumes that the potential-field data are harmonic. Therefore, these data must be previously processed and some considerations must be done in order to make this assumption valid.

Equation 26 cannot be used in practical applications because we never have a continuous record of a potential-field representing a harmonic function  $U(x, y, z)$ . Rather, we have a discrete set of potential-field observations  $d_i^o$ ,  $i = 1, \dots, N$ , in which  $d_i^o \equiv U(x_i, y_i, z_i)$  is the  $i$ th potential-field data at the  $i$ th coordinate point  $(x_i, y_i, z_i)$ , i.e.:

$$d_i^o = \frac{1}{2\pi} \int_{-\infty}^{+\infty} \int_{-\infty}^{+\infty} \frac{(z_c - z_i) U(x, y, z_c)}{[(x_i - x)^2 + (y_i - y)^2 + (z_i - z_c)^2]^{\frac{3}{2}}} dx dy, \quad z_c > z_i. \quad (27)$$

According to this equation, the potential-field observation  $d_i^o$  is proportional to the convolution between  $U(x, y, z_c)$  and the vertical derivative of the function  $1/r$  (equation 10), both evaluated on the horizontal plane at  $z = z_c$  (Figure 2). From the physical point of view, this



convolution represents the scalar potential produced by a continuous double layer having vertical moment and intensity equal to  $-U(x, y, z_c)/2\pi$ . It means that all the potential-field data  $d_i^o$ ,  $i = 1, \dots, N$ , located at the observation points  $(x_i, y_i, z_i)$ , where  $z_i < z_c$ , can be exactly reproduced by the same continuous dipole layer at the horizontal plane  $z = z_c$ .

By assuming the knowledge of the continuous function  $U(x, y, z_c)$  (Equation 27), it is possible to calculate the potential field at all observation points located above the continuous double layer. In other words, we can determine  $N$  potential-field observations  $d_i^o$ ,  $i = 1, \dots, N$ , each one computed at a different observation point  $(x_i, y_i, z_i)$  placed anywhere above the horizontal plane at  $z = z_c$ , thus  $z_i < z_c$ . Hence, the potential-field observations can be calculated on an irregular grid of points and on an uneven surface, such as the Earth's surface for a ground survey or a draped surface for an airborne survey. Theoretically, this continuous layer can also be used to calculate the derivatives as well as other potential-field transformations.

## Discrete equivalent layer

One of the simplest solutions of the integral equation 27 can be obtained numerically by

$$d_i^o \approx \sum_{j=1}^M \left\{ \left( \frac{\Delta S_j d_j}{2\pi} \right) \frac{(z_c - z_i)}{[(x_i - x)^2 + (y_i - y)^2 + (z_i - z_c)^2]^{\frac{3}{2}}} \right\}, \quad z_c > z_i, \quad (28)$$

where  $\Delta S_j$  is an element of area of the numerical integration and  $d_j \equiv U(x_j, y_j, z_c)$  is the potential-field at a coordinate point  $(x_j, y_j, z_c)$ ,  $j = 1, \dots, M$ , located on the horizontal plane with  $z = z_c$  (Figure 2). However, from a set of  $N$  potential-field observations  $d_i^o$  (equation 27),  $i = 1, \dots, N$ , there will also be infinite solutions  $U(x, y, z_c)$  that satisfy equation 27. This is an ill-posed problem because, as pointed out by Parker (1977), the observations lie in a finite  $N$ -dimensional space whereas the solution lies in an infinite-dimensional space of

functions. Among the infinite possible solutions  $U(x, y, z_c)$ , we can choose a particular one given by a linear combination of  $M$  harmonic functions  $g(x - x_j, y - y_j, z_c - z_j)$  as follows

$$U(x, y, z_c) \approx \sum_{j=1}^M p_j g(x - x_j, y - y_j, z_c - z_j), \quad (29)$$

where  $p_j$ ,  $j = 1, \dots, M$ , are the constant coefficients. Besides being harmonic, the functions  $g(x - x_j, y - y_j, z_c - z_j)$ ,  $j = 1, \dots, M$ , must be regular and tends to zero as the distance between the points  $(x, y, z_c)$  and  $(x_j, y_j, z_j)$  tends to infinite. Notice that, if the  $M$  harmonic functions  $g(x - x_j, y - y_j, z_c - z_j)$  in equation 29 are linearly independent, they form a basis for an  $M$ -dimensional space and, consequently, the constant coefficients  $p_j$  approximating  $U(x, y, z_c)$  are unique. By inserting the linear combination of harmonic functions (equation 29) into the discrete form of the upward continuation integral (equation 27), we have

$$d_i^o \approx \frac{1}{2\pi} \int_{-\infty}^{+\infty} \int_{-\infty}^{+\infty} \frac{(z_c - z_i)}{[(x_i - x)^2 + (y_i - y)^2 + (z_i - z_c)^2]^{\frac{3}{2}}} \sum_{j=1}^M p_j g(x - x_j, y - y_j, z_c - z_j) dx dy. \quad (30)$$

Because the  $M$  coefficients  $p_j$  do not depend on the integration variables, we can rewrite equation 30 as

$$d_i^o \approx \sum_{j=1}^M p_j \left\{ \frac{1}{2\pi} \int_{-\infty}^{+\infty} \int_{-\infty}^{+\infty} \frac{(z_c - z_i) g(x - x_j, y - y_j, z_c - z_j)}{[(x_i - x)^2 + (y_i - y)^2 + (z_i - z_c)^2]^{\frac{3}{2}}} dx' dy' \right\}. \quad (31)$$

Now, by defining the new variables  $\epsilon = x - x_j$ ,  $\eta = y - y_j$  and  $\zeta = z_j - z_c$  and substituting them into equation 31, we obtain

$$d_i^o \approx \sum_{j=1}^M p_j \left\{ \frac{1}{2\pi} \int_{-\infty}^{+\infty} \int_{-\infty}^{+\infty} \frac{(\zeta - (z_i - z_j)) g(\epsilon, \eta, \zeta)}{[(x_i - x_j) - \epsilon]^2 + ((y_i - y_j) - \eta)^2 + ((z_i - z_j) - \zeta)^2]^{\frac{3}{2}}} d\epsilon d\eta \right\}. \quad (32)$$

Notice that the term between brackets in equation 32 is similar to equation 27, showing that

$$g(x_i - x_j, y_i - y_j, z_i - z_j) = \frac{1}{2\pi} \int_{-\infty}^{+\infty} \int_{-\infty}^{+\infty} \frac{(\zeta - (z_i - z_j)) g(\epsilon, \eta, \zeta)}{[(x_i - x_j) - \epsilon]^2 + ((y_i - y_j) - \eta)^2 + ((z_i - z_j) - \zeta)^2]^{\frac{3}{2}}} d\epsilon d\eta, \quad (33)$$

which represents the upward continuation of the harmonic function  $g(x_i - x_j, y_i - y_j, z_i - z_j)$ . Similarly to equation 27, equation 33 shows that  $g(x_i - x_j, y_i - y_j, z_i - z_j)$  can be obtained from its values on a horizontal plane with constant vertical coordinate  $z = \zeta$ . Finally, by substituting equation 33 into equation 32, we obtain

$$d_i^o \approx \sum_{j=1}^M p_j g(x_i - x_j, y_i - y_j, z_i - z_j), \quad (34)$$

which could be thought of as generalization of equation 28. This approach for deducing equation 34 is based on Mendonça (1992) and shows that the potential-field data  $d_i^o$ , at the observation point  $(x_i, y_i, z_i)$ ,  $i = 1, \dots, N$ , can be approximated by a linear combination of  $M$  harmonic functions  $g(x_i - x_j, y_i - y_j, z_i - z_j)$ . This linear combination in turn is also a harmonic function. These harmonic functions can be considered the potential field produced by a discrete layer of  $M$  equivalent sources located at the coordinates  $(x_j, y_j, z_j)$ ,  $j = 1, \dots, M$ .

Notice that the problem of determining the continuous function  $U(x, y, z_c)$  which describes the physical property distribution within a continuous double layer (equation 27) can be approximated by the problem of defining the harmonic functions  $g(x_i - x_j, y_i - y_j, z_i - z_j)$  and estimating the constant coefficients  $p_j$  (equation 34) which describe a discrete layer of equivalent sources. In the geophysical literature, this technique of estimating the parameters describing a discrete layer of equivalent sources which reproduce the potential-field data measured at a finite set of observation points is named either equivalent source technique or equivalent layer technique. Here, we opted for using the second term.

### Classical equivalent layer

The classical equivalent layer approach consists in solving a linear inverse problem to estimate the constant coefficients  $p_j$ ,  $j = 1, \dots, M$  (equation 34), describing a discrete layer of

equivalent sources. Let the observed data vector be defined by  $\mathbf{d}^o$ , whose  $i$ th element  $d_i^o$ ,  $i = 1, \dots, N$ , represents a potential-field observation at the point  $(x_i, y_i, z_i)$ . From equation 34, the observed data  $d_i^o$  can be approximated by a linear combination of harmonic functions given by

$$d_i^p(\mathbf{p}) = \sum_{j=1}^M p_j g_{ij}, \quad (35)$$

where  $\mathbf{p}$  is an  $M \times 1$  vector whose  $j$ th element  $p_j$  can represent the scalar physical property of the  $j$ th equivalent source located at the position  $(x_j, y_j, z_j)$  and  $g_{ij} \equiv g(x_i - x_j, y_i - y_j, z_i - z_j)$  (equation 34),  $j = 1, \dots, M$ . Equation 35 can be written in matrix notation as follows

$$\mathbf{d}^p(\mathbf{p}) = \mathbf{G}\mathbf{p}, \quad (36)$$

where  $\mathbf{d}^p(\mathbf{p})$  is the predicted data vector, whose  $i$ th element  $d_i^p(\mathbf{p})$ ,  $i = 1, \dots, N$ , is the potential-field data produced by the linear combination of  $M$  equivalent sources (equation 35) and  $\mathbf{G}$  is an  $N \times M$  dense matrix whose  $ij$ th element is the harmonic (Green's) function  $g_{ij}$  (equation 35). The harmonic function  $g_{ij}$  represents the potential field produced, at position  $(x_i, y_i, z_i)$ , by an equivalent source located at position  $(x_j, y_j, z_j)$  and having unitary (scalar) physical property. The classical approach consists in estimating the parameter vector  $\mathbf{p}$  by solving the linear inverse problem of minimizing the difference between the observed data  $\mathbf{d}^o$  and the predicted data  $\mathbf{d}^p(\mathbf{p})$  (equation 36). To obtain a stable estimate  $\mathbf{p}^*$ , this linear inverse problem is generally constrained by using a regularization function (Tikhonov and Arsenin, 1977). For example, a stable estimate  $\mathbf{p}^*$  can be obtained by minimizing the goal function

$$\Gamma(\mathbf{p}) = \Psi(\mathbf{p}) + \mu \Omega(\mathbf{p}), \quad (37)$$

where the first term  $\Psi(\mathbf{p})$  is the data misfit function given by

$$\Psi(\mathbf{p}) = \|\mathbf{d}^o - \mathbf{d}^p(\mathbf{p})\|_2^2, \quad (38)$$

which is the squared Euclidean norm of the difference between the observed data  $\mathbf{d}^o$  and the predicted data  $\mathbf{d}^p(\mathbf{p})$  (equation 36), and  $\mu$  is a positive real number controlling the trade-off between the data misfit function and the zeroth-order Tikhonov regularization (Tikhonov and Arsenin, 1977; Aster et al., 2005) given by

$$\Omega(\mathbf{p}) = \|\mathbf{p}\|_2^2, \quad (39)$$

which is the squared Euclidean norm of the parameter vector  $\mathbf{p}$ .

After obtaining a stable estimate  $\mathbf{p}^*$ , a desired linear transformation, such as interpolation, reduction to the pole and upward (or downward) continuation, is performed by

$$\mathbf{d}'(\mathbf{p}^*) = \mathbf{T} \mathbf{p}^*, \quad (40)$$

where  $\mathbf{d}'(\mathbf{p}^*)$  is an  $L \times 1$  vector whose  $k$ th element  $d'_k(\mathbf{p}^*)$  is the transformed-potential field at position  $(x_k, y_k, z_k)$ ,  $k = 1, \dots, L$ . We stress that the transformed potential-field data are calculated at  $L$  points  $(x_k, y_k, z_k)$ ,  $k = 1, \dots, L$ , which are not necessarily coincident with the  $N$  observation points  $(x_i, y_i, z_i)$ ,  $i = 1, \dots, N$ . Finally,  $\mathbf{T}$  is an  $L \times M$  matrix whose  $kj$ th element  $t_{kj}$  is an harmonic (Green's) function representing the desired transformed-potential field produced by the  $j$ th equivalent source with unitary physical property at the  $k$ th point  $(x_k, y_k, z_k)$ .

## Matrix $\mathbf{G}$

The harmonic functions  $g_{ij}$  (equation 35) forming the matrix  $\mathbf{G}$  (equation 36) can describe the potential field produced by different kinds of equivalent sources. These functions, however, must be harmonic and vanish as the distance to the source increases. As pointed out by Li et al. (2014), the physical relationship between the equivalent sources and the

potential-field data produced by them can or cannot be the same physical relationship between the true (magnetic or gravity) sources and the observed potential-field data. Table 1 shows the kind of equivalent-sources, the mathematical/physical meaning of the harmonic functions describing the potential field produced by them as well as the observed potential-field data used by several authors. As shown in this table, Dampney (1969) approximated a observed Bouguer anomaly by the vertical component of the gravitational attraction exerted by point masses, preserving the physical relationship between the observed potential field data and their actual sources. On the other hand, Cordell (1992) and Guspí and Novara (2009), for example, used different approaches in which the physical relationship between the observed potential field data and their actual sources is released. Cordell (1992) approximated an observed Bouguer anomaly by the gravitational potential produced by point masses whereas Guspí and Novara (2009) approximated a total-field anomaly by the second directional derivative of a generic harmonic function representing a higher-order potential produced by point sources.

Here, we exemplify the formulations of the equivalent layer technique for processing and/or interpreting gravity disturbance (or Bouguer anomaly) data and total-field anomaly data. For convenience, we limit our examples to the cases in which observed gravity data are approximated by the vertical component of the gravitational attraction exerted by point masses, and the case in which observed total-field anomaly is approximated by the total-field anomaly produced by dipoles.

The harmonic functions  $g_{ij}$  (equation 35) describing the potential field produced by point masses and dipoles, as well as the harmonic functions describing the transformed-potential field  $t_{kj}$  (equation 40) produced by them, can be written in terms of the inverse distance function  $\theta_j(x, y, z)$ , its first derivatives  $\frac{\partial \theta_j(x_i, y_i, z_i)}{\partial \alpha} \equiv \partial_\alpha \theta_{ij}$ , second derivatives  $\frac{\partial^2 \theta_j(x_i, y_i, z_i)}{\partial \alpha \partial \beta} \equiv$

$\partial_{\alpha\beta}\theta_{ij}$ , and third derivatives  $\frac{\partial^3\theta_j(x_i,y_i,z_i)}{\partial\alpha\partial\beta\partial\gamma} \equiv \partial_{\alpha\beta\gamma}\theta_{ij}$ , where  $\alpha = x, y, z$ ,  $\beta = x, y, z$ ,  $\gamma = x, y, z$ .

The inverse distance function  $\theta_j(x, y, z)$  is given by

$$\theta_j(x, y, z) = \frac{1}{r_j}, \quad (41)$$

whereas its derivatives are given by

$$\partial_{\alpha}\theta_{ij} = \frac{\alpha_j - \alpha_i}{r_j^3}, \quad (42)$$

$$\partial_{\alpha\beta}\theta_{ij} = \begin{cases} \frac{3(\alpha_i - \alpha_j)^2}{r_j^5} + \frac{1}{r_j^3}, & \alpha = \beta \\ \frac{3(\alpha_i - \alpha_j)(\beta_i - \beta_j)}{r_j^5}, & \alpha \neq \beta \end{cases}, \quad (43)$$

and

$$\partial_{\alpha\beta\gamma}\theta_{ij} = \begin{cases} \frac{9(\alpha_i - \alpha_j)}{r_j^5} - \frac{15(\alpha_i - \alpha_j)^3}{r_j^7}, & \alpha = \beta = \gamma \\ \frac{3(\gamma_i - \gamma_j)}{r_j^5} - \frac{15(\alpha_i - \alpha_j)^2(\gamma_i - \gamma_j)}{r_j^7}, & \alpha = \beta \neq \gamma \\ \frac{15(\alpha_i - \alpha_j)(\beta_i - \beta_j)(\gamma_i - \gamma_j)}{r_j^7}, & \alpha \neq \beta, \alpha \neq \gamma, \beta \neq \gamma \end{cases}, \quad (44)$$

where

$$r_j = [(x - x_j)^2 + (y - y_j)^2 + (z - z_j)^2]^{\frac{1}{2}} \quad (45)$$

represents the Euclidean distance between the observation point  $(x, y, z)$  and the position  $(x_j, y_j, z_j)$  of the  $j$ th equivalent source and  $\alpha = x, y, z$ ,  $\beta = x, y, z$ ,  $\gamma = x, y, z$ . The derivatives shown in equations 42, 43 and 44 are computed with respect to the coordinates  $x$ ,  $y$  and  $z$  of the observation point.

The harmonic functions  $g_{ij}$ ,  $j = 1, \dots, M$  (equation 35), describing the vertical component of the gravitational attraction exerted by point masses can be defined as follows:

$$g_{ij} \equiv c_g \partial_z \theta_{ij}, \quad (46)$$

where  $c_g$  and  $\partial_z \theta_{ij}$  are defined in equations 1 and 42, respectively. By using such harmonic functions (equation 46), the predicted data  $d_i^p(\mathbf{p})$  (equation 35) can be written as

$$d_i^p(\mathbf{p}) = c_g \sum_{j=1}^M p_j \partial_z \theta_{ij}, \quad (47)$$

and the  $j$ th constant coefficient  $p_j$ ,  $j = 1, \dots, M$  (equation 35), can be considered the mass (in kg) of the  $j$ th equivalent source.

The harmonic functions  $g_{ij}$ ,  $j = 1, \dots, M$  (equation 35), describing the total-field anomaly produced by dipoles can be defined as follows:

$$g_{ij} \equiv c_m \hat{\mathbf{F}}^\top \mathbf{H}_{ij} \hat{\mathbf{h}}, \quad (48)$$

where  $\hat{\mathbf{F}}$  is the unit vector (equation 5) having the same direction as the local-geomagnetic field  $\mathbf{F}_0$  (equation 3),  $c_m$  is the constant defined in equation 6,  $\hat{\mathbf{h}}$  is a constant unit vector given by

$$\hat{\mathbf{h}} = \begin{bmatrix} \cos(I) \cos(D) \\ \cos(I) \sin(D) \\ \sin(I) \end{bmatrix}_{3 \times 1}, \quad (49)$$

which represents the arbitrary magnetization direction with constant inclination  $I$  and constant declination  $D$  of all dipoles forming the equivalent layer and the matrices  $\mathbf{H}_{ij}$  are given by

$$\mathbf{H}_{ij} = \begin{bmatrix} \partial_{xx} \theta_{ij} & \partial_{xy} \theta_{ij} & \partial_{xz} \theta_{ij} \\ \partial_{xy} \theta_{ij} & \partial_{yy} \theta_{ij} & \partial_{yz} \theta_{ij} \\ \partial_{xz} \theta_{ij} & \partial_{yz} \theta_{ij} & \partial_{zz} \theta_{ij} \end{bmatrix}_{3 \times 3}, \quad (50)$$

where the second derivatives  $\partial_{\alpha\beta} \theta_{ij}$ ,  $\alpha = x, y, z$ ,  $\beta = x, y, z$ , are defined in equation 43. By using such harmonic functions (equation 48), the  $j$ th constant coefficient  $p_j$ ,  $j = 1, \dots, M$  (equation 35), can be considered the magnetic moment intensity (in  $\text{Am}^2$ ) of the  $j$ th equivalent source. For convenience, the unit vector  $\hat{\mathbf{h}}$  (equations 48 and 49) can also be written



as

$$\hat{\mathbf{h}} = \mathbf{R}\hat{\mathbf{m}}, \quad (51)$$

where  $\hat{\mathbf{m}}$  (equation 8) is a unit vector with the same direction as the true magnetization of the source and  $\mathbf{R}$  is a  $3 \times 3$  matrix obtained from Euler's rotation theorem. This theorem states that any rotation can be parametrized by using three parameters called Euler angles (Goldstein et al., 1980). Notice that, if the equivalent sources have the same magnetization direction as the true magnetic source, the rotation matrix  $\mathbf{R}$  (equation 51) is equal to the identity matrix. Finally, by using the harmonic functions  $g_{ij}$  defined in equation 48 and the unit vector  $\hat{\mathbf{h}}$  shown in equation 51, the predicted data  $d_i^p(\mathbf{p})$  (equation 35) can be written as

$$d_i^p(\mathbf{p}) = c_m \hat{\mathbf{F}}^\top \left( \sum_{j=1}^M p_j \mathbf{H}_{ij} \right) \mathbf{R}\hat{\mathbf{m}}. \quad (52)$$

## Computational aspects

Generally, the linear inverse problem of estimating a stable parameter vector  $\mathbf{p}^*$  minimizing the goal function (equation 37) deals with a large and dense matrix  $\mathbf{G}$  (equation 36). Consequently, this problem deals with large-scaled matrix computations, making the equivalent layer technique computationally inefficient. As properly pointed out by Barnes and Lumley (2011), the key to a successful application of the equivalent layer rests with carefully designed algorithm that can handle large-scaled problems efficiently and reliably. Any algorithm designed to solve problems involving large-scaled matrix computations needs to take advantage of the particular structure of these matrices instead of using strategies that were developed for general matrices. The performance of an algorithm can be increased, for example, by exploiting the fact that a symmetric matrix can be stored in half the space of a general matrix or by designing matrix-vector products that consider only the nonzero

entries (Press et al., 1992; Golub and Loan, 2013). The computational efficiency of an algorithm depends, amongst other factors, on the amount of required arithmetic and storage. A way of determining the amount of required arithmetic is by counting the number of floating-point operations (*flops*), which is the number of additions, subtractions, multiplications or divisions of floating-point numbers (Boyd and Vandenberghe, 2004; Golub and Loan, 2013).

A stable estimate  $\mathbf{p}^*$  minimizing the goal function (equation 37) can be obtained, for example, by using an overdetermined formulation (Menke, 1989)

$$\mathbf{p}^* = \left( \mathbf{G}^\top \mathbf{G} + \mu \mathbf{I} \right)^{-1} \mathbf{G}^\top \mathbf{d}^o \quad (53)$$

or an underdetermined formulation

$$\mathbf{p}^* = \mathbf{G}^\top \left( \mathbf{G} \mathbf{G}^\top + \mu \mathbf{I} \right)^{-1} \mathbf{d}^o. \quad (54)$$

Notice that, in equation 53,  $\mathbf{I}$  is the  $M \times M$  identity matrix, whereas in equation 54,  $\mathbf{I}$  is the  $N \times N$  identity matrix. While the linear system to be solved in equation 53 contains an  $M \times M$  matrix  $(\mathbf{G}^\top \mathbf{G} + \mu \mathbf{I})$ , the one to be solved in equation 54 contains an  $N \times N$  matrix  $(\mathbf{G} \mathbf{G}^\top + \mu \mathbf{I})$ . The number of *flops* needed to construct the linear systems shown in equations 53 and 54 are, respectively,

$$f_c^o = M^2 N + M + 2MN \quad (55)$$

and

$$f_c^u = M N^2 + N + 2MN. \quad (56)$$

Here, by regarding the symmetry of the matrices involved, we consider that the solution of the linear systems are obtained from the Cholesky factorization. In this case, the number of *flops* needed to solve the linear systems shown in equations 53 and 54 are, respectively,

$$f_s^o = \frac{1}{3} M^3 + 2M^2 \quad (57)$$

and

$$f_s^u = \frac{1}{3}N^3 + 2N^2. \quad (58)$$

Generally, the number of equivalent sources  $M$  are greater than the number of potential-field data  $N$  and, therefore, the overdetermined solution (equation 53) is more computationally expensive than the underdetermined solution (equation 54). Figure 3a shows a graph of the ratio  $M/N$  versus the ratio  $f_c^o/f_c^u$  (equations 55 and 56). Figure 3b shows a graph of the ratio  $M/N$  versus the ratio  $f_s^o/f_s^u$  (equations 57 and 58). Although these graphs were calculated for a fixed  $N = 10000$ , we can verify that they are almost independent of  $N$  for  $N > 100$ . According to Figure 3a, if the number  $M$  of equivalent sources is six times greater than the number  $N$  of potential-field data, the number of *flops*  $f_c^o$  (equation 55) is approximately six times greater than the number of *flops*  $f_c^u$  (equation 56). Similarly, Figure 3b shows that, for this same ratio  $M/N = 6$ , the number of *flops*  $f_s^o$  (equation 57) is approximately two hundred times greater than the number of *flops*  $f_s^u$  (equation 58).

Several authors have developed different algorithms to improve the computational efficiency of the equivalent layer technique. Leão and Silva (1989) developed a fast method for processing a regular grid of potential-field data. The method consists in estimating an equivalent layer which exactly reproduces the potential-field data within a small data window. The data window is shifted over the whole gridded data set in a procedure similar to a discrete convolution. The equivalent layer extends beyond the moving-data window and is located at a depth between two and six times the grid spacing of the observations. For each data window, the equivalent layer is estimated by solving an underdetermined linear system similar to that one presented in equation 54. After estimating an equivalent layer, the transformed-potential field is computed only at the center of the moving-data window. The use of a small moving-data window greatly reduces the total number of *flops*

and memory storage. The computational efficiency of this method relies on the strategy of constructing the equivalent layer by successively solving small linear systems instead of solving just one large linear system for the entire equivalent layer. Mendonça and Silva (1994) also followed the strategy of solving successive small linear systems for constructing an equivalent layer. Their method is based on the equivalent-data concept, which consists in determining a subset of all potential-field data (named equivalent-data set), such that the interpolating surface that fits the chosen subset also automatically fits all remaining data. The equivalent data set is obtained by iteratively introducing the potential-field observation with the greatest residual in the preceding iteration. By applying to the interpolation problem, the method is optimized by approximating dot products by the discrete form of an analytic integration that can be evaluated with less computational effort. According to the authors, the equivalent-data set is usually smaller than the total number of potential-field observations, leading to computational savings. The authors also pointed out that the computational efficiency of the method depends on the number of equivalent data. If the potential-field anomaly is nonsmooth, the number of equivalent data can be large and the method will be less efficient than the classical approach.

By following a different strategy, Li and Oldenburg (2010) developed a rapid method that transforms the dense matrix  $\mathbf{G}$  (equation 36) into a sparse one by using a wavelet technique. After obtaining a sparse representation of the matrix  $\mathbf{G}$ , these authors estimate the physical-property distribution within the equivalent layer by using an overdetermined formulation similar to that one shown in equation 53. These authors pointed out that, given the sparse representation, their method reduces the computational time required for solving the linear system by as many as two orders of magnitude if compared with the same formulation using a dense matrix. Barnes and Lumley (2011) followed a similar strategy

and transformed the dense matrix  $\mathbf{G}$  (equation 36) into a sparse one. However, differently from Li and Oldenburg (2010), their method operates in the space domain by grouping equivalent sources far from an observation point into blocks with average physical property. This procedure aims at reducing the memory storage and achieving computational efficiency by solving the transformed linear system with a weighted-least-squares conjugate-gradient algorithm. Notice that, instead of constructing the equivalent layer by solving successive small linear systems, these last two methods first transform the large linear system into a sparse one and then take advantage of this sparseness.

Oliveira Jr. et al. (2013) developed a fast method based on the reparameterization of the physical-property distribution within the equivalent layer. These authors divided the equivalent layer into a regular grid of equivalent-source windows inside which the physical-property distribution is described by bivariate polynomial functions. By using this polynomial representation, the inverse problem of constructing the equivalent layer is posed in the space of the total number of polynomial coefficients within all equivalent-source windows instead of in the space of the total number of equivalent sources. According to Oliveira Jr. et al. (2013), the computational efficiency of their method relies on the fact that the total number of polynomial coefficients needed to describe the physical property distribution within the equivalent layer is generally much smaller than the number of equivalent sources, leading to a very smaller linear system to be solved. These authors could verify that the total number of *flops* needed for building and solving the linear inverse problem of estimating the total number of polynomial coefficients can be reduced by as many as three and four orders of magnitude, respectively, if compared with the same inverse problem of estimating the physical property of each equivalent source forming the equivalent layer.

The method presented by Cordell (1992) and after generalized by Guspí and Novara

(2009) does not estimate the physical property distribution within the equivalent layer by solving a linear system. The physical property of the sources, which are located below each potential-field data, are iteratively updated by a procedure that removes the maximum residual between the observed and predicted data. The total number of *flops* required by these iterative methods for estimating the physical-property distribution within the equivalent layer depends on the total number of iterations, however this number is generally much smaller than the total number of *flops* required to solve a large-scaled linear system. Generally, the most computational expensive step in each iteration of these methods is the forward problem of calculating the potential-field data produced by the equivalent layer.

## A REVIEW AND GENERALIZATION OF THEORETICAL ASPECTS CONCERNING THE EQUIVALENT LAYER

Despite the equivalent layer concept be grounded on well-established potential-field theory, the theoretical aspects of this method have received little attention. Much less attention has been given to the estimated physical-property distribution within an equivalent layer.

By following different approaches in the wavenumber domain, the pioneers Pedersen (1991) and Li et al. (2014) determined the magnetic moment distribution within a continuous equivalent layer whose magnetization is parallel to a vertical local-geomagnetic field. These authors considered a planar equivalent layer which is parallel to a horizontal plane containing the observed total-field anomaly. They also considered that the magnetization of the source is aligned with the local-geomagnetic field. Under these assumptions, Pedersen (1991) and Li et al. (2014) concluded that the magnetic moment distribution within the continuous equivalent layer is proportional to the pseudogravity anomaly produced by the

source on the plane of the equivalent layer.

Here, we present, in the space domain, a mathematical analysis of the relationship between the estimated magnetic moment distribution within a planar equivalent layer and the magnetization direction of its equivalent sources. Different from the previous works, our analysis neither assumes that the observed magnetic anomaly is produced by a purely induced magnetization nor imposes that magnetization direction of the equivalent sources within the equivalent layer is aligned with the inducing field.

Let's first consider a stable magnetic moment distribution  $p_j^*$ ,  $j = 1, \dots, M$ , within a planar equivalent layer having arbitrary magnetization direction. By considering that this stable magnetic moment distribution yields an acceptable data fitting, we obtain from equations 8 and 52 that

$$m \mathbf{M}_i \approx \sum_{j=1}^M p_j^* \mathbf{H}_{ij} \mathbf{R}. \quad (59)$$

This equation can be simplified if the magnetization direction of all dipoles forming the equivalent layer is equal to the direction of the true magnetic source. In this particular case, the rotation matrix  $\mathbf{R}$  (equations 51 and 52) is equal to the identity matrix and we obtain

$$m \mathbf{M}_i \approx \sum_{j=1}^M p_j^\dagger \mathbf{H}_{ij}, \quad (60)$$

where the particular magnetic moment distribution  $p_j^\dagger$  is different from the magnetic moment distribution  $p_j^*$ ,  $j = 1, \dots, M$ , shown in equation 59. Theoretically, equation 60 shows that this particular magnetic moment distribution is unique because it is a linear combination of linearly independent functions. Equation 60 shows that

$$m \partial_{\alpha\beta} \phi_i \approx \sum_{j=1}^M p_j^\dagger \partial_{\alpha\beta} \theta_{ij}, \quad (61)$$

where  $\alpha = x, y, z$ ,  $\beta = x, y, z$ ,  $\partial_{\alpha\beta} \phi_i$  are the second derivatives forming the matrix  $\mathbf{M}$

(equation 7) and  $\partial_{\alpha\beta}\theta_{ij}$  are the second derivatives forming the matrix  $\mathbf{H}_{ij}$  (equation 50).

We remark that the magnetic moment distribution  $p_j^\dagger$ ,  $j = 1, \dots, M$ , which satisfies equation 61 for a particular  $\alpha\beta$  must equally satisfies this equation for all the remaining  $\alpha\beta$ . Then, without loss of generality, we consider the case in which

$$m \partial_{zz}\phi_i \approx \sum_{j=1}^M p_j^\dagger \partial_{zz}\theta_{ij} , \quad (62)$$

where  $\partial_{zz}\phi_i$  is the second derivative, evaluated at the observation point  $(x_i, y_i, z_i)$ ,  $i = 1, \dots, N$ , of the harmonic function  $\phi(x, y, z)$  (equation 2) with respect to the variable  $z$ . In this case, the integral (equation 2) is conducted over the volume of the magnetic source.

To proceed with our analysis of the magnetic moment distribution within a planar equivalent layer, we conveniently define the function  $\partial_{zz}\phi_i$  (equation 62) as the derivative, evaluated at the observation point  $(x_i, y_i, z_i)$ ,  $i = 1, \dots, N$ , of the harmonic function  $\partial_z\phi_i$  with respect to the variable  $z$ . The harmonic function  $\partial_z\phi_i$ , in turn, represents the first derivative of the function  $\phi(x, y, z)$  (equation 2) with respect to the variable  $z$ . We know from potential theory that any harmonic function satisfies the upward continuation integral (equations 26 and 27), therefore  $\partial_z\phi_i$  can be written as follows

$$\partial_z\phi_i = \int_{-\infty}^{+\infty} \int_{-\infty}^{+\infty} \left( \frac{\partial_z\phi}{2\pi} \right) \frac{z_c - z_i}{[(x_i - x)^2 + (y_i - y)^2 + (z_i - z_c)^2]^{\frac{3}{2}}} dx dy , \quad z_c > z_i , \quad (63)$$

where  $\partial_z\phi$  represents the first derivative, evaluated on the plane  $z = z_c$  (Figure 2), of the function  $\phi(x, y, z)$  (equation 2) with respect to the variable  $z$ .

Notice that, in equation 63, the function  $\partial_z\phi_i$  is evaluated at the observation point  $(x_i, y_i, z_i)$  and the  $\partial_z\phi$  is evaluated at a point located on the horizontal plane with constant vertical coordinate  $z = z_c$  (Figure 2). Hence, by deriving both sides of equation 63 with



respect to the variable  $z$  of the observation point, we obtain

$$\partial_{zz}\phi_i = \int_{-\infty}^{+\infty} \int_{-\infty}^{+\infty} \left( \frac{\partial_z \phi}{2\pi} \right) \frac{3(z_c - z_i)^2 + [(x_i - x)^2 + (y_i - y)^2 + (z_i - z_c)^2]^2}{[(x_i - x)^2 + (y_i - y)^2 + (z_i - z_c)^2]^{\frac{5}{2}}} dx dy, \quad z_c > z_i. \quad (64)$$

This equation can be solved by numerical integration as follows

$$\partial_{zz}\phi_i \approx \sum_{j=1}^M \left( \frac{\Delta S_j \partial_z \phi_j}{2\pi} \right) \partial_{zz}\theta_{ij}, \quad (65)$$

where  $\Delta S_j$  is an element of area,  $\partial_z \phi_j$  is the first derivative of the function  $\phi(x, y, z)$  (equation 2) with respect to the variable  $z$  and  $\partial_{zz}\theta_{ij}$  is given by equations 43 and 45. In this approximation, both  $\partial_z \phi_j$  and  $\partial_{zz}\theta_{ij}$  are evaluated on discrete points  $(x_j, y_j, z_j)$  located on the horizontal plane with  $z_j = z_c > z_i$  (Figure 2).

To analyse the physical meaning of equation 65, first recall that  $\partial_z \phi_j$  is proportional to the gravity disturbance  $\delta g_j$  (equation 1),  $j = 1, \dots, M$ , that would be produced by the magnetic source, on the horizontal plane at  $z_c$  (Figure 2), if it had a positive and constant density  $\rho = 1/G$ , where  $G$  is the Newtonian constant of gravitation. Additionally, if we multiply both sides of equation 65 by the magnetization intensity  $m$  of the source, we obtain

$$m \partial_{zz}\phi_i \approx \sum_{j=1}^M \left( \frac{\Delta S_j m \delta g_j}{2\pi \rho c_g} \right) \partial_{zz}\theta_{ij}, \quad (66)$$

where  $c_g$  is a constant defined in equation 1. Finally, it is then noticeable from equations 62 and 66 that

$$p_j^\dagger \approx \left( \frac{\Delta S_j m}{2\pi \rho c_g} \right) \delta g_j, \quad j = 1, \dots, M. \quad (67)$$

This relationship is similar to that presented by Pedersen (1991) and Li et al. (2014) between the magnetic moment distribution  $p_j^\dagger$  within a planar equivalent layer and the pseudogravity on the equivalent layer. However, we do not follow the same wavenumber-domain reasoning used by these authors. In contrast, the magnetic moment distribution  $p_j^\dagger$  deduced in

equation 67 takes a magnetization direction of the equivalent sources within the equivalent layer equal to that one of the true magnetic source. Moreover, the observed total-field anomaly can be measured on an uneven surface and be produced by a set of magnetic sources having the same arbitrary magnetization direction. Hence, equation 67 generalizes the previous relationships because it (1) does not impose an induced magnetization of the equivalent sources within the equivalent layer, (2) does not assume that the observed magnetic anomaly is produced by a purely induced magnetization and, (3) does not consider the observed total-field anomaly on a horizontal plane.

Because all constants within the parenthesis in equation 67 are positive, we can see that, if the equivalent sources have a magnetization with the same direction as the true magnetization of the sources, the estimated magnetic moment distribution within the equivalent layer will be all positive and reach the maximum values over the sources. Li et al. (2014) cleverly took advantage of this all-positive physical property distribution and solved the linear inverse problem of the equivalent layer by imposing a positivity constraint. Their approach for proving the existence an all-positive physical property distribution, however, is valid only for the case in which the observed total-field anomaly is produced by magnetic sources having a purely induced magnetization. Equation 67 generalizes this positivity condition because our approach holds true for all cases in which the magnetization of the equivalent sources has the same direction as the true magnetization of the sources, whenever it is purely induced or not.

## APPLICATIONS

In this section we present a numerical validation of the theoretical magnetic moment distribution deduced in the previous section (equation 67) and also demonstrate the power of

the equivalent layer technique in processing potential-field data. This is accomplished by using the synthetic data produced by the two rectangular prisms shown in Figure 4. The smaller one has the top at 0.05 km and side lengths equal to 2 km, 2 km and 1.95 km along, respectively, the  $x$ -,  $y$ - and  $z$ -axis. The greater prism has the top at 0.1 km and side lengths equal to 2 km, 6 km and 2 km along the  $x$ -,  $y$ - and  $z$ -axis, respectively.

### **Validation of the theoretical magnetic-moment distribution**

We present a numerical validation of the theoretical magnetic-moment distribution which is given by equation 67 and depends on the gravity data (not show) that would be produced by the true magnetic sources, on the plane containing the equivalent sources, if they had a density equal to  $1/G$ , where  $G$  is the Newtonian gravitational constant. Figure 5 shows the undulating surface (in grayscale) containing the points (black dots) on which the noise-free total-field anomaly data (Figure 6a) produced by the synthetic prisms (Figure 4) were calculated. The data are located on a regular grid of  $90 \times 90$  points with a grid spacing of  $0.33708 \times 0.33708$  km in the north-south and east-west directions, respectively. The simulated geomagnetic field has inclination  $6^\circ$  and declination  $-40.5^\circ$ . We set up 3,600 equivalent sources (dipoles) distributed on a regular grid of  $90 \times 90$  in the north-south and east-west directions, respectively, at constant depth of -0.079 km. Figure 6b shows the total-field anomaly produced by an equivalent layer with the theoretical magnetic-moment distribution shown in Figure 6c and calculated with equation 67. Notice that the total-field anomaly produced by this equivalent layer retrieves not only the noise-free total-field anomaly (Figure 6a) very well but also produces a reduced-to-the-pole anomaly (Figure 7b) very close to the true one (Figure 7a). Moreover, notice that the theoretical magnetic-moment distribution within the equivalent layer (Figure 6c) is all positive, which is in

accordance with our mathematical analysis.

### **Transformations that do not depend on the physical property distribution**

We illustrate the use of the equivalent layer technique in interpolating gravity data and upward-continuing magnetic data. These two transformations do not require the knowledge of any parameter describing to the physical property distribution within the true sources. The simulated potential-field observations produced by the two prisms (Figure 4) were calculated on a regular grid of  $120 \times 30$  observation points (black dots in Figure 8) with a grid spacing of  $0.252 \times 1.034$  km in the north-south and east-west directions, respectively.

#### *Interpolation*

Figure 9a shows the corrupted gravity data (vertical component of the gravitational attraction) with a pseudorandom Gaussian noise having zero mean and 1 mGal standard deviation. By using the classical equivalent layer technique (equation 53), these observations were interpolated in a regular grid of  $120 \times 29$  points (red dots in Figure 8) located between the observation points (black dots in Figure 8), on the same undulating surface (grayscale map in Figure 8). We set up 3,600 equivalent sources (point masses) distributed on a regular grid of  $120 \times 30$  in the north-south and east-west directions, respectively, at constant depth of -0.198 km. Figure 9b shows the interpolated gravity data. The difference between the interpolated and the true noise-free (not shown) gravity data is obtained at each grid point. The histogram of these differences (Figure 9c) confirms the good performance of the equivalent layer technique as an interpolation method.

### *Upward continuation*

Figure 10a shows, in grayscale, the corrupted total-field anomaly with a pseudorandom Gaussian noise having zero mean and 5 nT standard deviation. We set up 3,600 equivalent sources (dipoles) distributed on a regular grid of  $120 \times 30$  in the north-south and east-west directions, respectively, at constant depth of -0.198 km. The magnetization direction of these dipoles is equal to that one of the simulated geomagnetic field (inclination  $6^\circ$  and declination  $-40.5^\circ$ ), which is different from the magnetization direction of the true sources (Figure 4). In this case, the rotation matrix  $\mathbf{R}$  (equations 51, 52 and 59) is different from the identity matrix. Figure 10b shows, in grayscale, the upward-continued total-field anomaly at a planar surface with constant vertical coordinate -1.4 km. The histogram of the differences between the upward-continued and the true noise-free (not shown) total-field anomalies (Figure 10c) at this planar surface shows the good performance of the equivalent layer technique in producing an upward-continued data. This result also shows that the upward continuation is a potential-field data transformation that does not depend on the knowledge of the magnetization direction of the true sources.

### **Transformations that depend on the physical property distribution**

We illustrate the use of the equivalent layer technique to reduce the noise-corrupted total-field anomaly (Figure 10a) to the pole. This is an example of a potential-field data transformation that depends on the knowledge of the magnetization direction of the sources. We set up 3,600 equivalent sources (dipoles) distributed on a regular grid of  $120 \times 30$  in the north-south and east-west directions, respectively, at constant depth of -0.079 km. We present two tests aiming at estimating reduced-to-the-pole anomalies close to the true total-

field anomaly at the pole (Figure 11a). In both tests, the simulated geomagnetic field has inclination  $6^\circ$  and declination  $-40.5^\circ$ .

In the first one, the magnetization direction of the dipoles are equal to the magnetization direction of the true sources (Figure 4). In this case, the rotation matrix  $\mathbf{R}$  (equations 51, 52 and 59) is equal to the identity matrix. Figure 11b shows the reduced-to-the-pole anomaly yielded by the estimated magnetic-moment distribution (Figure 11c) within the equivalent layer. Notice that this estimated magnetic-moment distribution is very close to the theoretical magnetic-moment distribution shown in Figure 6c, which is in perfect agreement with our mathematical analysis (equations 59-67). This result also shows that, by using dipoles with the same magnetization direction of the true sources, we obtained a reduced-to-the-pole anomaly (Figure 11b) very close to the true total-field anomaly at the pole (Figure 11a).

In the second test, we set to all dipoles forming the equivalent layer a magnetization direction with the same inclination and declination of the geomagnetic field, which is different from the magnetization direction of the true sources (Figure 4). In this case, the rotation matrix  $\mathbf{R}$  (equations 51, 52 and 59) is different from the identity matrix. Figure 12a shows the reduced-to-the-pole anomaly yielded by the estimated magnetic-moment distribution (Figure 12b) within the equivalent layer. Notice that this estimated magnetic-moment distribution is very different from the theoretical magnetic-moment distribution shown in Figure 6c, confirming our mathematical analysis. As can be seen, this reduced-to-the-pole anomaly presents significant differences if compared to the true total-field anomaly at the pole (Figure 11a). This result illustrates a well-known concept that the use of equivalent sources having a wrong magnetization direction (e.g., a magnetization direction different from that one of the true sources) yields to a wrong reduced-to-the-pole anomaly (Figure

12a).

## SUMMARY

The mathematical base of equivalent layer technique dates back to around the 19th century, However, in the geophysics literature it was not used until the second half of the 20th century to process and to interpret potential-field data. Due to its high computational demands, the equivalent layer technique has only raised moderate interest of geophysicists. In the beginning, the feasibility of using the equivalent layer technique to process potential-field surveys with a limited number of observations was greatly explored. Next, by following different approaches, the computational aspects of the equivalent layer technique were improved to make feasible the equivalent layer technique for processing large data sets. Surprisingly, since the beginning of using the equivalent layer technique, its theoretical aspects have received little attention. More recently, the theoretical aspect of the physical-property estimate within the equivalent layer has been addressed. For example, the relationship between the estimated magnetic moment distribution within the continuous equivalent layer and the pseudogravity anomaly produced by the source on the plane of the equivalent layer was recently addressed by assuming restrictions such as a purely induced magnetization. We present, in the space domain, a sound generalization of this relationship between the magnetic moment distribution within a planar equivalent layer and the gravity data. This generalization allows us to prove that a positive physical-property distribution within an equivalent layer exists even if the magnetic data are produced by remanent magnetization.

Currently, the equivalent layer technique is mostly used to process potential-field data. However, we call attention that it has also been employed indirectly in interpretation. This occurs if the desired transformation of the potential-field data depends on the physical-

property distribution within the equivalent layer. In this case the interpreter needs to know information about the causative sources to perform the transformation of the data via equivalent layer technique. In reducing the magnetic data to the pole, for example, the interpreter needs to know the magnetization direction of the sources; otherwise the reduction fails. If the interpreter does not know, different hypotheses about the magnetization direction of the sources can be tried to estimate a soundly reduced-to-the-pole data. In this way, the interpreter can use the equivalent layer technique to interpret the physical property of the causative sources. It is expected that the next decade the equivalent layer technique be widely used not only in processing but also in interpreting potential-field data. To make the equivalent layer technique feasible to interpret potential field data, its computational efficiency still needs to be improved.



## REFERENCES

- Aster, R. C., B. Borchers, and C. H. Thurber, 2005, Parameter estimation and inverse problems (international geophysics): Academic Press.
- Barnes, G., 2014, Reconstructing the gravity gradient anomaly field from surveys with wide line spacing using equivalent source processing: an error analysis: *Geophysical Prospecting*, **62**, 646–657.
- Barnes, G., and J. Lumley, 2011, Processing gravity gradient data: *GEOPHYSICS*, **76**, I33–I47.
- Baumann, H., E. Klingelé, and I. Marson, 2012, Absolute airborne gravimetry: a feasibility study: *Geophysical Prospecting*, **60**, 361–372.
- Bhattacharyya, B. K., 1967, Some general properties of potential fields in space and frequency domain: a review: *Geoexploration*, **5**, 127–143.
- Bhattacharyya, B. K., and K. C. Chan, 1977, Reduction of magnetic and gravity data on an arbitrary surface acquired in a region of high topographic relief: *Geophysics*, **42**, 1411–1430.
- Blakely, R. J., 1996, *Potential theory in gravity and magnetic applications*: Cambridge University Press.
- Bott, M. H. P., 1967, Solution of the linear inverse problem in magnetic interpretation with application to oceanic magnetic anomalies: *Geophysical Journal of the Royal Astronomical Society*, **13**, 313–323.
- Bott, M. H. P., and A. Ingles, 1972, Matrix methods for joint interpretation of two-dimensional gravity and magnetic anomalies with application to the iceland-faeroe ridge: *Geophysical Journal of the Royal Astronomical Society*, **30**, 55–67.
- Boyd, S., and L. Vandenberghe, 2004, *Convex optimization*: Cambridge University Press.

- Cordell, L., 1992, A scattered equivalent-source method for interpolation and gridding of potentialfield data in three dimensions: *GEOPHYSICS*, **57**, 629–636.
- Dampney, C. N. G., 1969, The equivalent source technique: *GEOPHYSICS*, **34**, 39–53.
- Daneš, Z. F., 1962, Structure calculations from gravity data and density logs: *Transactions of the Society of Mining Engineers of AIME*, **223**, 23–29.
- Davis, K., and Y. Li, 2011, Fast solution of geophysical inversion using adaptive mesh, space-filling curves and wavelet compression: *Geophysical Journal International*, **185**, 157–166.
- Emilia, D. A., 1973, Equivalent sources used as an analytic base for processing total magnetic field profiles: *GEOPHYSICS*, **38**, 339–348.
- Glennie, C. L., K. P. Schwarz, A. M. Bruton, R. Forsberg, A. V. Olesen, and K. Keller, 2000, A comparison of stable platform and strapdown airborne gravity: *Journal of Geodesy*, **74**, 383–389.
- Goldstein, H., C. P. Poole Jr., and J. L. Safko, 1980, *Classical mechanics*, 3 ed.: Addison-Wesley.
- Golub, G. H., and C. F. V. Loan, 2013, *Matrix computations* (johns hopkins studies in the mathematical sciences): Johns Hopkins University Press.
- Gunn, P. J., 1975, Linear transformations of gravity and magnetic fields: *Geophysical Prospecting*, **23**, 300–312.
- Guspi, F., and I. Novara, 2009, Reduction to the pole and transformations of scattered magnetic data using newtonian equivalent sources: *GEOPHYSICS*, **74**, L67–L73.
- Hackney, R. I., and W. E. Featherstone, 2003, Geodetic versus geophysical perspectives of the gravity anomaly: *Geophysical Journal International*, **154**, 35–43.
- Hansen, R. O., and Y. Miyazaki, 1984, Continuation of potential fields between arbitrary

- surfaces: *GEOPHYSICS*, **49**, 787–795.
- Henderson, R. G., 1960, A comprehensive system of automatic computation in magnetic and gravity interpretation: *GEOPHYSICS*, **25**, 569–585.
- , 1970, On the validity of the use of the upward continuation integral for total magnetic intensity data: *GEOPHYSICS*, **35**, 916–919.
- Henderson, R. G., and I. Zietz, 1949, The upward continuation of anomalies in total magnetic intensity fields: *GEOPHYSICS*, **14**, 517–534.
- Hofmann-Wellenhof, B., and H. Moritz, 2005, *Physical geodesy*: Springer.
- Kellogg, O. D., 1929, *Foundations of potential theory*: Frederick Ungar Publishing Company.
- Leão, J. W. D., and J. B. C. Silva, 1989, Discrete linear transformations of potential field data: *GEOPHYSICS*, **54**, 497–507.
- Li, Y., M. Nabighian, and D. W. Oldenburg, 2014, Using an equivalent source with positivity for low-latitude reduction to the pole without striation: *GEOPHYSICS*, **79**, J81–J90.
- Li, Y., and D. W. Oldenburg, 2010, Rapid construction of equivalent sources using wavelets: *GEOPHYSICS*, **75**, L51–L59.
- MacLennan, K., and Y. Li, 2013, Denoising multicomponent csem data with equivalent source processing techniques: *Geophysics*, **78**, E125–E135.
- Mayhew, M. A., 1982, Application of satellite magnetic anomaly data to curie isotherm mapping: *Journal of Geophysical Research: Solid Earth*, **87**, 4846–4854.
- Mendonça, C. A., 1992, *Interpolação de dados de campo potencial através da camada equivalente*: PhD thesis, Universidade Federal do Pará, Belém do Pará, Brazil.
- Mendonça, C. A., and J. B. C. Silva, 1994, The equivalent data concept applied to the interpolation of potential field data: *GEOPHYSICS*, **59**, 722–732.

- Menke, W., 1989, Geophysical data analysis: Discrete inverse theory: Academic Press, Inc.
- Nabighian, M. N., M. E. Ander, V. J. S. Grauch, R. O. Hansen, T. R. LaFehr, Y. Li, W. C. Pearson, J. W. Peirce, J. D. Phillips, and M. E. Ruder, 2005a, Historical development of the gravity method in exploration: *GEOPHYSICS*, **70**, 63ND–89ND.
- Nabighian, M. N., V. J. S. Grauch, R. O. Hansen, T. R. LaFehr, Y. Li, J. W. Peirce, J. D. Phillips, and M. E. Ruder, 2005b, The historical development of the magnetic method in exploration: *GEOPHYSICS*, **70**, 33ND–61ND.
- Oliveira Jr., V. C., V. C. F. Barbosa, and L. Uieda, 2013, Polynomial equivalent layer: *GEOPHYSICS*, **78**, G1–G13.
- Parker, R. L., 1977, Understanding inverse theory: *Annual Review of Earth and Planetary Sciences*, **5**, 35–64.
- Pawlowski, R. S., 1994, Greens equivalent-layer concept in gravity bandpass filter design: *GEOPHYSICS*, **59**, 69–76.
- Pedersen, L. B., 1991, Relations between potential fields and some equivalent sources: *GEO-PHYSICS*, **56**, 961–971.
- Pilkington, M., and W. E. S. Urquhart, 1990, Reduction of potential field data to a horizontal plane: *GEOPHYSICS*, **55**, 549–555.
- Press, W. H., B. P. Flannery, S. A. Teukolsky, and W. T. Vetterling, 1992, Numerical recipes in c: The art of scientific computing, second edition: Cambridge University Press.
- Roy, A., 1962, Ambiguity in geophysical interpretation: *GEOPHYSICS*, **27**, 90–99.
- Silva, J. B. C., 1986, Reduction to the pole as an inverse problem and its application to low-latitude anomalies: *GEOPHYSICS*, **51**, 369–382.
- Skeels, D. C., 1947, Ambiguity in gravity interpretation: *GEOPHYSICS*, **12**, 43–56.
- Tikhonov, A. N., and V. Y. Arsenin, 1977, Solutions of ill-posed problems: V. H. Winston

& Sons.

Twomey, S., 1977, Introduction to the mathematics of inversion in remote sensing and indirect measurements: Dover Publications, Inc.

Von Frese, R. R. B., W. J. Hinze, and L. W. Braile, 1981, Spherical earth gravity and magnetic anomaly analysis by equivalent point source inversion: Earth and Planetary Science Letters, **53**, 69 – 83.

Xia, J., D. R. Sprowl, and D. Adkins-Heljeson, 1993, Correction of topographic distortions in potential-field data; a fast and accurate approach: GEOPHYSICS, **58**, 515–523.

Zidarov, D., 1965, Solution of some inverse problems of applied geophysics: Geophysical Prospecting, **13**, 240–246.

## LIST OF FIGURES

1 2D representation of a 3D regular region with volume  $v$  and boundary defined by a regular surface  $S$ , whose outward normal is represented by  $\hat{\mathbf{n}}$ .  $x_i$ ,  $y_i$  and  $z_i$  are the coordinates of a point located within  $v$ . These coordinates are referred to a Cartesian system with the  $x$  axis pointing into the page, the  $y$  axis pointing to right and the  $z$  axis pointing downward.

2 2D representation of a 3D regular region with volume  $v$  and boundary defined by the union of a hemisphere  $S_1$  with radius  $R$  and a horizontal plane  $S_2$  at the vertical coordinate  $z = z_c$ .  $\hat{\mathbf{n}}_1$  and  $\hat{\mathbf{n}}_2$  represent, respectively, the normal to the surfaces  $S_1$  and  $S_2$ . The points  $(x_i, y_i, z_i)$  and  $(x_i, y_i, z_s)$  are located, respectively, inside and outside  $v$ . These points are located at the same distance from the horizontal plane  $S_2$ , so that  $z_i = z_c - \Delta z$  and  $z_s = z_c + \Delta z$ . The coordinates are referred to a Cartesian system with the  $x$  axis pointing into the page, the  $y$  axis pointing to right and the  $z$  axis pointing downward.

3 (a) Graph of the ratio  $M/N$  versus the ratio  $f_c^o/f_c^u$  (equations 55 and 56). (b) Graph of the ratio  $M/N$  versus the ratio  $f_s^o/f_s^u$  (equations 57 and 58).  $N$  represents the number of potential-field data and  $M$  represents the number of parameters (equivalent sources) to be estimated by solving the linear systems 53 and 54.

4 Synthetic bodies with constant density  $\rho = 1000 \text{ kg/m}^3$  and constant magnetization vector with intensity  $m = 10 \text{ A/m}$ , inclination  $30^\circ$  and declination  $-10^\circ$ . The geomagnetic field has  $6^\circ$  inclination and  $-40.5^\circ$  declination.

5 Undulating surface (grayscale) on which we calculate the noise-free total-field anomaly data (Figure 6a) produced by the simulated prisms shown in Figure 4. The white rectangles represent the horizontal projection of the simulated prisms and the black dots represent the horizontal location of the observation points.

6 (a) Noise-free total-field anomaly produced by the simulated prisms (Figure 4) at the observation points (black dots in Figure 5). (b) Total-field anomaly produced by a planar equivalent layer with the theoretical magnetic-moment distribution given by equation 67. (c) Theoretical magnetic-moment distribution calculated by using equation 67 within the equivalent layer. The black and white rectangles represent the horizontal projection of the simulated prisms.

7 (a) True total-field anomaly at the pole produced by the simulated prisms (Figure 4) at the observation points located on the undulating surface shown in Figure 5. (b) Reduced-to-the-pole anomaly produced by the planar equivalent layer with the theoretical magnetic-moment distribution shown in Figure 6c. The white rectangles represent the horizontal projection of the simulated prisms.

8 Undulating surface (grayscale) on which we calculate the noise-corrupted gravity (Figure 9a) and magnetic (Figure 10a) data produced by the simulated prisms shown in Figure 4. The white rectangles represent the horizontal projection of the simulated prisms, the black dots represent the horizontal location of the observation points and the red dots represent the horizontal location of the interpolated points.

9 (a) Noise-corrupted gravity data produced by the simulated prisms (Figure 4) at the observation points (black dots in Figure 8). (b) Interpolated gravity data at the interpolated points (red dots in Figure 8). (c) Histogram of the differences between the interpolated and the true noise-free (not shown) gravity data. The differences are transformed in a dimensionless variable  $Z$  by subtracting each difference from the sample mean  $\mu$  and then dividing the difference by the sample standard deviation  $\sigma$ . The black and white rectangles represent the horizontal projection of the simulated prisms.

10 (a) Noise-corrupted total-field anomaly produced by the simulated prisms (Figure 4) on the observation points (black dots in Figure 8). (b) Upward-continued total-field anomaly at a planar surface with vertical coordinate -1.4 km. (c) Histogram of the differences between the upward-continued and the true noise-free (not shown) total-field anomalies. The differences are transformed in a dimensionless variable  $Z$  by subtracting each difference from the sample mean  $\mu$  and then dividing the difference by the sample standard deviation  $\sigma$ . The black rectangles represent the horizontal projection of the simulated prisms.

11 (a) True total-field anomaly at the pole produced by the simulated prisms (Figure 4) at the observation points located on the undulating surface shown in Figure 8. (b) Reduced-to-the-pole anomaly at the observation points (black dots in Figure 8). (c) Estimated magnetic-moment distribution within the equivalent layer by using equivalent sources with the same magnetization direction of the simulated prisms (i.e., inclination  $30^\circ$  and declination  $-10^\circ$ ). The white rectangles represent the horizontal projection of the simulated prisms.

12 (a) Reduced-to-the-pole anomaly on the undulating surface (grayscale in Figure 8) (b) Estimated magnetization-intensity distribution within the equivalent layer wrongly assuming that the sources are magnetized by the induction only. The magnetization direction of the dipoles that make up the equivalent layer is the same of the geomagnetic field (i.e., inclination  $6^\circ$  and declination  $-40.5^\circ$ ). The white rectangles represent the horizontal projection of the simulated prisms.

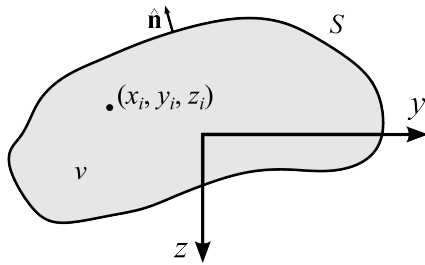


Figure 1: 2D representation of a 3D regular region with volume  $v$  and boundary defined by a regular surface  $S$ , whose outward normal is represented by  $\hat{\mathbf{n}}$ .  $x_i$ ,  $y_i$  and  $z_i$  are the coordinates of a point located within  $v$ . These coordinates are referred to a Cartesian system with the  $x$  axis pointing into the page, the  $y$  axis pointing to right and the  $z$  axis pointing downward.



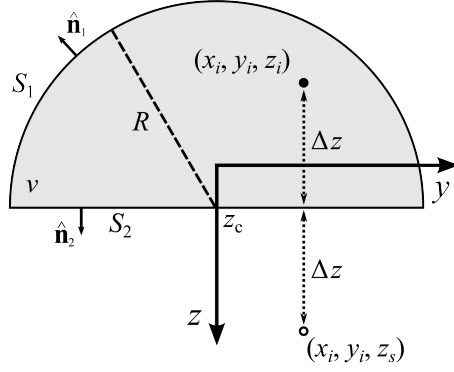


Figure 2: 2D representation of a 3D regular region with volume  $v$  and boundary defined by the union of a hemisphere  $S_1$  with radius  $R$  and a horizontal plane  $S_2$  at the vertical coordinate  $z = z_c$ .  $\hat{\mathbf{n}}_1$  and  $\hat{\mathbf{n}}_2$  represent, respectively, the normal to the surfaces  $S_1$  and  $S_2$ . The points  $(x_i, y_i, z_i)$  and  $(x_i, y_i, z_s)$  are located, respectively, inside and outside  $v$ . These points are located at the same distance from the horizontal plane  $S_2$ , so that  $z_i = z_c - \Delta z$  and  $z_s = z_c + \Delta z$ . The coordinates are referred to a Cartesian system with the  $x$  axis pointing into the page, the  $y$  axis pointing to right and the  $z$  axis pointing downward.

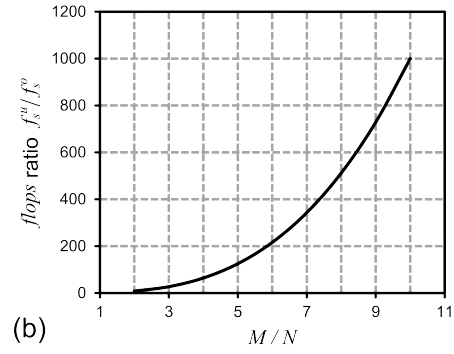
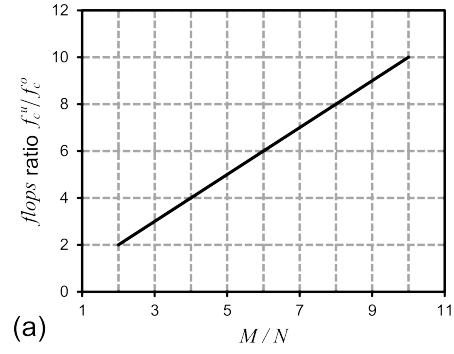


Figure 3: (a) Graph of the ratio  $M/N$  versus the ratio  $f_c^o/f_c^u$  (equations 55 and 56). (b) Graph of the ratio  $M/N$  versus the ratio  $f_s^o/f_s^u$  (equations 57 and 58).  $N$  represents the number of potential-field data and  $M$  represents the number of parameters (equivalent sources) to be estimated by solving the linear systems 53 and 54.

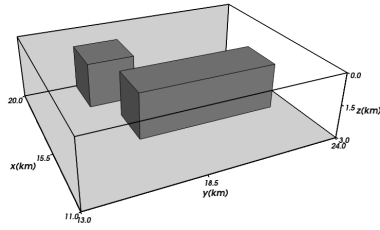


Figure 4: Synthetic bodies with constant density  $\rho = 1000 \text{ kg/m}^3$  and constant magnetization vector with intensity  $m = 10 \text{ A/m}$ , inclination  $30^\circ$  and declination  $-10^\circ$ . The geomagnetic field has  $6^\circ$  inclination and  $-40.5^\circ$  declination.

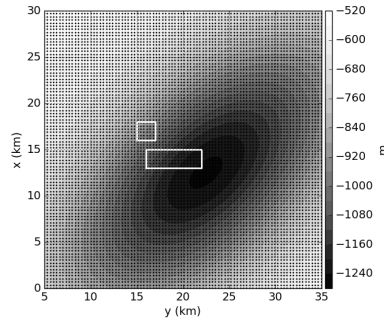


Figure 5: Undulating surface (grayscale) on which we calculate the noise-free total-field anomaly data (Figure 6a) produced by the simulated prisms shown in Figure 4. The white rectangles represent the horizontal projection of the simulated prisms and the black dots represent the horizontal location of the observation points.

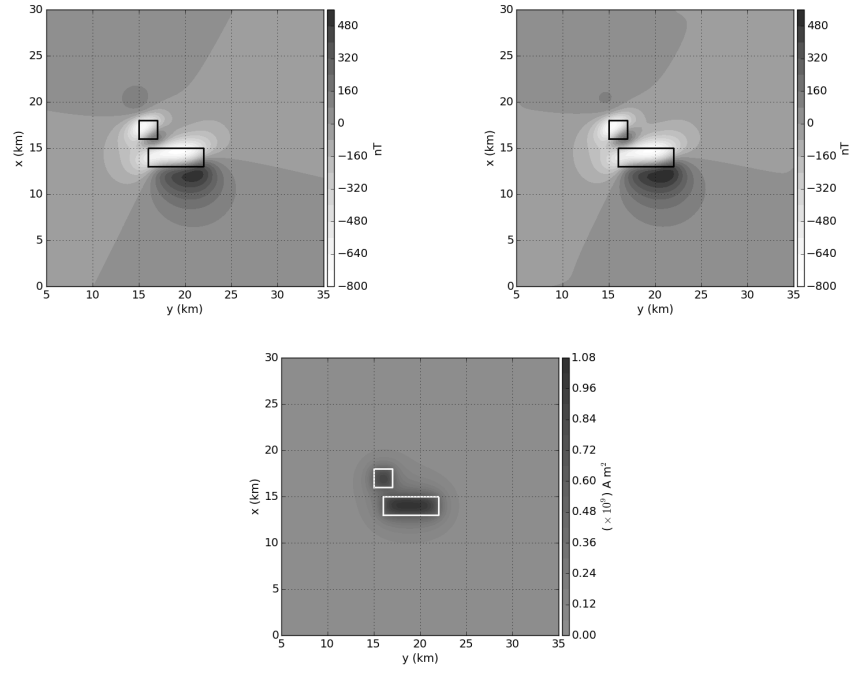


Figure 6: (a) Noise-free total-field anomaly produced by the simulated prisms (Figure 4) at the observation points (black dots in Figure 5). (b) Total-field anomaly produced by a planar equivalent layer with the theoretical magnetic-moment distribution given by equation 67. (c) Theoretical magnetic-moment distribution calculated by using equation 67 within the equivalent layer. The black and white rectangles represent the horizontal projection of the simulated prisms.

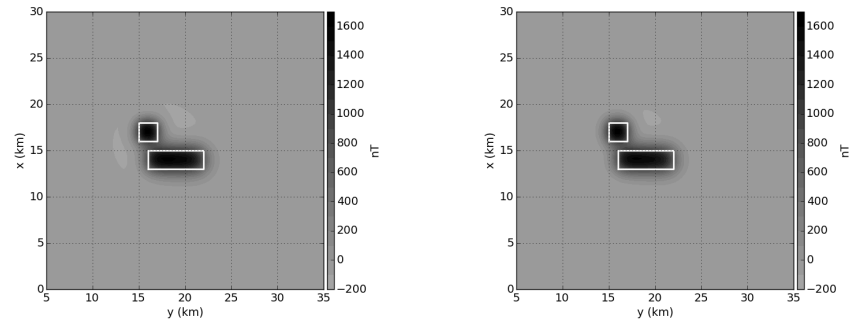


Figure 7: (a) True total-field anomaly at the pole produced by the simulated prisms (Figure 4) at the observation points located on the undulating surface shown in Figure 5. (b) Reduced-to-the-pole anomaly produced by the planar equivalent layer with the theoretical magnetic-moment distribution shown in Figure 6c. The white rectangles represent the horizontal projection of the simulated prisms.

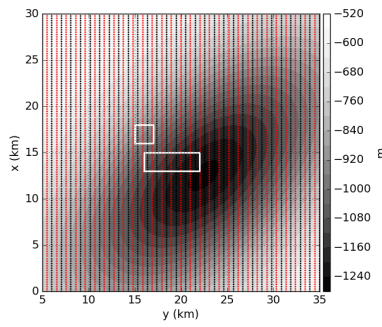


Figure 8: Undulating surface (grayscale) on which we calculate the noise-corrupted gravity (Figure 9a) and magnetic (Figure 10a) data produced by the simulated prisms shown in Figure 4. The white rectangles represent the horizontal projection of the simulated prisms, the black dots represent the horizontal location of the observation points and the red dots represent the horizontal location of the interpolated points.

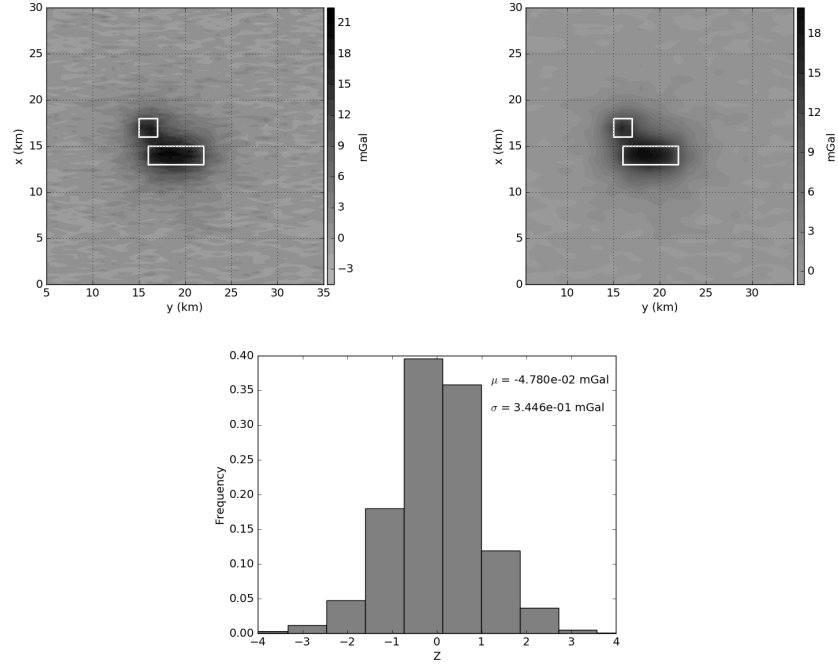


Figure 9: (a) Noise-corrupted gravity data produced by the simulated prisms (Figure 4) at the observation points (black dots in Figure 8). (b) Interpolated gravity data at the interpolated points (red dots in Figure 8). (c) Histogram of the differences between the interpolated and the true noise-free (not shown) gravity data. The differences are transformed in a dimensionless variable  $Z$  by subtracting each difference from the sample mean  $\mu$  and then dividing the difference by the sample standard deviation  $\sigma$ . The black and white rectangles represent the horizontal projection of the simulated prisms.



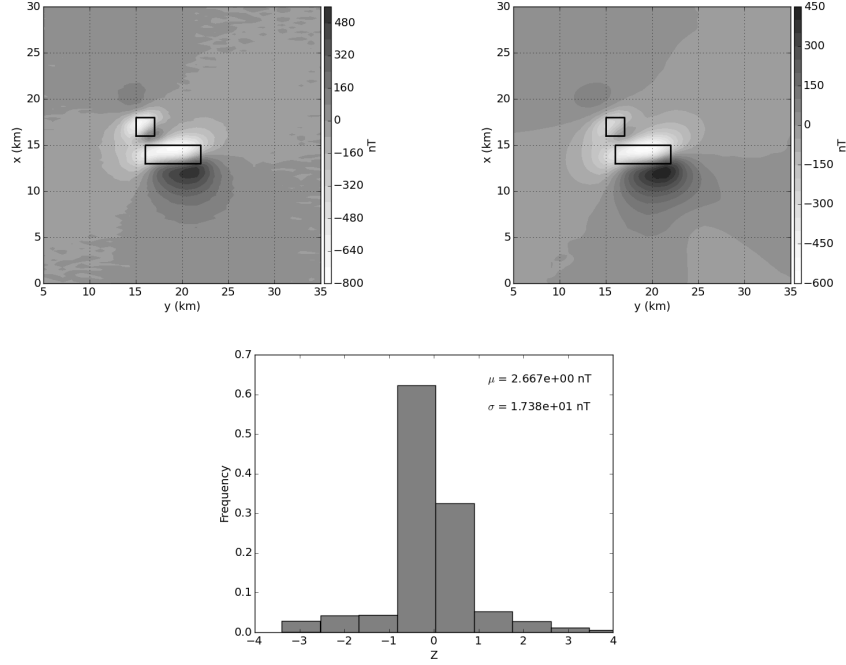


Figure 10: (a) Noise-corrupted total-field anomaly produced by the simulated prisms (Figure 4) on the observation points (black dots in Figure 8). (b) Upward-continued total-field anomaly at a planar surface with vertical coordinate -1.4 km. (c) Histogram of the differences between the upward-continued and the true noise-free (not shown) total-field anomalies. The differences are transformed in a dimensionless variable  $Z$  by subtracting each difference from the sample mean  $\mu$  and then dividing the difference by the sample standard deviation  $\sigma$ . The black rectangles represent the horizontal projection of the simulated prisms.

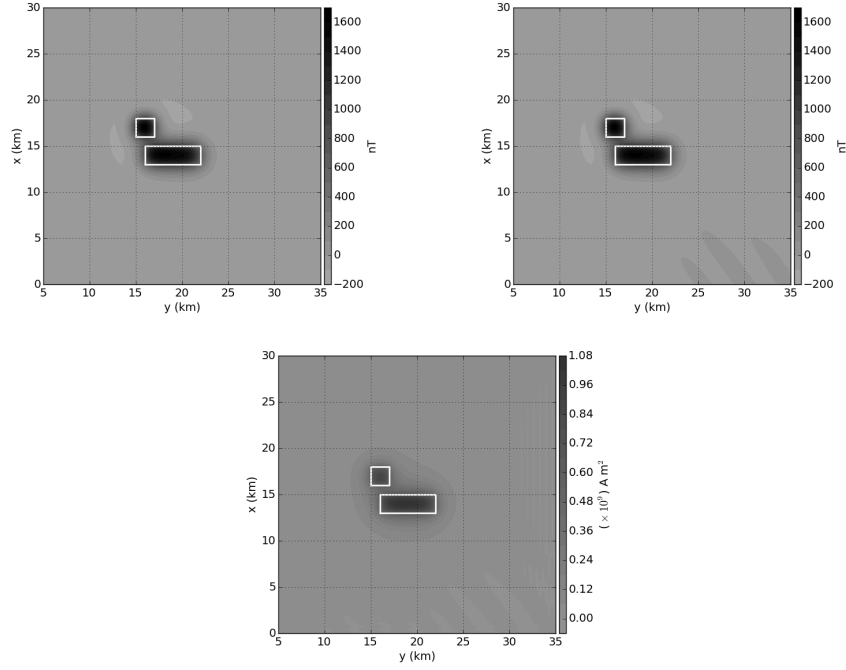


Figure 11: (a) True total-field anomaly at the pole produced by the simulated prisms (Figure 4) at the observation points located on the undulating surface shown in Figure 8. (b) Reduced-to-the-pole anomaly at the observation points (black dots in Figure 8). (c) Estimated magnetic-moment distribution within the equivalent layer by using equivalent sources with the same magnetization direction of the simulated prisms (i.e., inclination  $30^\circ$  and declination  $-10^\circ$ ). The white rectangles represent the horizontal projection of the simulated prisms.

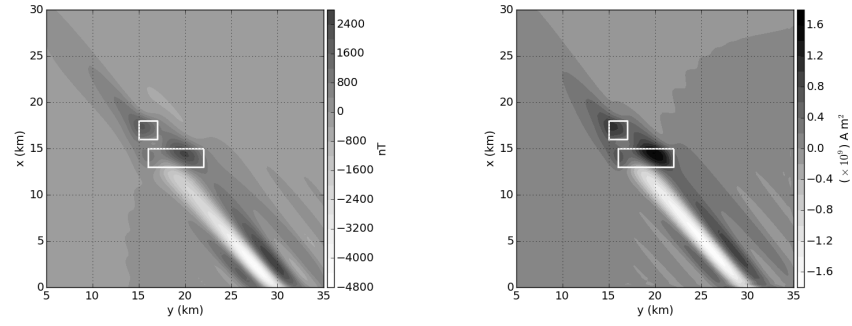


Figure 12: (a) Reduced-to-the-pole anomaly on the undulating surface (grayscale in Figure 8) (b) Estimated magnetization-intensity distribution within the equivalent layer wrongly assuming that the sources are magnetized by the induction only. The magnetization direction of the dipoles that make up the equivalent layer is the same of the geomagnetic field (i.e., inclination  $6^\circ$  and declination  $-40.5^\circ$ ). The white rectangles represent the horizontal projection of the simulated prisms.

## LIST OF TABLES

- 1 Observed potential-field data and the mathematical/physical meaning of the harmonic functions  $g_{ij}$  (equation 35) describing the potential field produced by the equivalent sources used by several authors.

Author(s)	Equivalent sources	Harmonic function $g_{ij}$	Observed data
Dampney (1969)	point masses	vertical component of the gravitational attraction	Bouguer anomaly
Emilia (1973)	lines of dipoles	total-field anomaly	total-field anomaly
Hansen and Miyazaki (1984)	uniformly-magnetized plane faces	magnetic scalar potential	total-field anomaly
Silva (1986)	doublets	total-field anomaly	total-field anomaly
Cordell (1992)	point masses	gravitational potential	Bouguer anomaly
Guspí and Novara (2009)	generic point sources producing a higher-order potential	second-directional derivative of the higher-order potential	total-field anomaly
Barnes and Lumley (2011)	rectangular prisms	second derivatives of the gravitational potential	gravity gradient
Oliveira Jr. et al. (2013)	dipoles	total-field anomaly	total-field anomaly
Li et al. (2014)	rectangular prisms	total-field anomaly	total-field anomaly

Table 1: Observed potential-field data and the mathematical/physical meaning of the harmonic functions  $g_{ij}$  (equation 35) describing the potential field produced by the equivalent sources used by several authors.